Increasingly complex systems in intense laser fields

Xiaoyan Ding

Thesis submitted to the University of Ottawa
in partial fulfillment of the requirements for the
Doctor of Philosophy degree in Physics

Department of Physics
Faculty of Science
University of Ottawa

Abstract

With more atoms in a system, coupling between quantum states complicates the system dynamics. We shine intense laser pulses on three systems with increasing complexity: a molecule, a dimer, and a solid.

For single molecules, a 400 nm photon excites NO_2 and initiates a dissociation process. We probe the dynamics using a strong laser pulse to ionize the molecule, and detect the resulting electrons and ions. The evolution of the NO-O molecular bond was directly measured in our experiment.

For dimers, a laser pulse removes three electrons from $(CO)_2$. The dimer breaks up into C^+, O^+ and CO^+. Compared to a monomer, CO^{2+} in the dimer has a new prompt dissociation pathway that produces fragments with higher kinetic energy. Calculation shows that the Coulomb field of the neighboring CO^+ modifies the electronic state of the dimer, giving rise to a prompt channel. Coupling between different charge state configurations results in a new dimer electronic state, which leads to dissociation with higher kinetic energy.

For solids, coupling among many atoms creates bands and a bandgap that plays the role of the ionization potential and reduces the threshold for electron-hole pair generation. Thus, solids are a good medium for high-order harmonic generation at the high repetition rates needed for frequency combs. We generate up to the 7th harmonic in silicon and zinc oxide with femtosecond pulses from a thulium fiber laser.

Acknowledgements

I would like to thank my supervisors, Dr. Paul Corkum and Dr. André Staudte. I am grateful that Dr. Paul Corkum accepted me to this fantastic group as a student and I thank both supervisors for their valuable guidance.

Thanks to Dr. Paul Corkum, Dr. André Staudte, Dr. David Villeneuve, Dr. Albert Stolow, Dr. Marko Haertelt, and Ruaridh Forbes for many discussions and ideas.

Thanks to Dr. André Staudte, Dr. Kevin F. Lee, Dr. Marko Haertelt, Dr. Matthias Kübel for teaching me experimental work and helping me with measurements. Dr. Marko Haertelt performed the measurements of $(CO)_2$ dimer in Chapter 4.

Thanks to Dr. Giulio Vampa and Dr. Kevin F. Lee for having me involved in the harmonics experiments. Dr. Giulio Vampa did the simulation for harmonics generation in solids at different laser intensities in Chapter 5. Dr. Kevin F. Lee built the Tm fiber laser and performed the experiment with me in Chapter 5.

Thanks to Dr. Michael Schuurman and Dr. Mike Spanner for their theoretical support. Dr. Schuurman calculated the potential energy surfaces of the CO^{2+} in a $(CO)_2$ dimer. Dr. Spanner estimated the dephasing time of NO_2 rotational wavepacket.

Thanks to Bert Avery, David Crane, Ryan Kroeker, and Dr. Andrei Naumov for their technical support. Thanks to Bert Avery and David Crane for dealing with the poisonous NO_2 gas, which kept me alive while using it.

Thanks to Dr. Paul Corkum, Dr. André Staudte, Zack Dube, and Dr. Kevin Lee for their help with editing this thesis.

Thanks to my family for their support throughout the years.

I acknowledge funding from the NSERC CREATE program through Dr. Paul Corkum.

Contents

List of Figures

Chapter 1

Introduction

In a complex system, some properties arise because of interactions among parts of the system and cannot be predicted by examining the individual parts themselves. This is called *emergence*. The most prominent example is the emergence of life within a sufficiently complex chemical system, with the whole being undeniably more than the individual molecular components. Emergent behaviors exist in various systems from molecules to human society, and even the formation of galaxies.

In this thesis, we study three systems with increasing complexity: a molecule, a dimer, and a solid. In each system we are studying a specific aspect of laser-matter interactions, all of which exhibit emergent phenomena. These phenomena become accessible through driving each system with a strong optical field.

First consider an atom. An electron in an atom is bound by the attractive Coulomb potential, as is shown by the black dashed curve in Fig. 1.1. When an atom is exposed to an intense laser pulse, the laser field lowers the potential barrier and the electron wavefunction will be partially ionized. This is called tunneling ionization. After ionization, the electron is driven by the laser field. The motion of the electron in the laser field can be described classically. If the driving laser pulse is circularly polarized, the electron is pulled away by the field in constantly changing directions and the wavepacket never returns to its parent ion. If the pulse is linearly polarized, the electron can return back to the parent ion if it is born at the right time during the laser cycle. This process is known as recollision.

Upon recollision, if the electron recombines with the ion, a photon is emitted with energy roughly equal to the sum of the electron wavepacket energy and the ionization potential [1]. If the driving laser pulse has many optical cycles, the generated photon

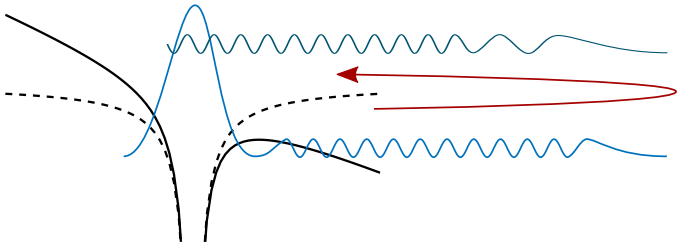

Figure 1.1: The electron wavepacket (blue Gaussian) is bound in an atom by Coulomb potential (dashed black line). An intense linearly polarized laser pulse lowers the potential energy barrier (solid black line). This allows the bound state electron wavefunction to tunnel and split, creating a wavepacket in the continuum. The wavepacket is driven by the oscillating laser field in a semiclassical trajectory (red arrow). It first accelerates away from the atom. As the laser field reverses, the electron accelerates back towards the parent ion.

energy is an odd multiple of the driving laser photon energy. This is the high harmonic generation process. If the electron has enough energy as it passes the ion, the ion can be collisionally ionized. Correlated two-electron ejection will be observed, known as the nonsequential double ionization (NSDI) [2]. The electron can also scatter elastically, resulting in high energy above threshold ionization (ATI) electrons [3].

Now consider a molecule. A molecule consists of two or more atoms and these atoms are held together through Coulomb attraction between the negatively charged electrons and positively charged nuclei. Rotation and vibration emerge from having more than one atom in the system. The complexity of even simple molecules still leaves many open questions [4]. These degrees of freedom are, for example, responsible for the atmospheric greenhouse effect [5]. The surface of the earth loses heat mostly through blackbody radiation, which is in the wavelength range of 5 - 50 μm. Rovibrational transitions in CO_2 allow the molecules to absorb around the wavelength of 15 μm [6], and therefore reduce the escape of radiation from the earth's surface and keep it warm.

Molecular dynamics can be investigated from many different perspectives, such as high harmonic generation [7, 8, 9], electron holography [10], time-resolved ATI spectroscopy [11], attosecond transient absorption spectroscopy [12]. In this thesis, we use a method called Coulomb explosion imaging (CEI) [13, 14, 15, 16, 17] to track nuclear motion. In an ideal Coulomb explosion, all the electrons in a molecule are removed instantaneously. The positively charged nuclei initially held together by the electrons will repel each other under the Coulomb interaction. The geometrical information of the molecule is imprinted onto the momentum of the fragment ions. By detecting the ions, we can reconstruct the geometry of the molecule. Coulomb explosion imaging measures one molecule per laser shot. It is a direct way to image nuclear dynamics. However,

removing all electrons is an ideal situation. In a real experiment, we remove a subset of all the electrons and the interaction between the ions is approximately Coulombic.

When molecules are cold enough, the attraction between transient dipoles, which arise from weak fluctuations in the charge distribution, can make them stick to one another. Such systems are called clusters, and the interactions between the component molecules are called van der Waals forces. What new phenomena beyond single molecules arise from the van der Waals interactions? For example, they are responsible for condensing water vapour into tiny droplets in clouds. Van der Waals interactions also play significant roles in biophysics, such as the interaction of proteins with other molecules [18].

A dimer is a van der Waals system containing only two component molecules. One emergent behavior in dimers is called intermolecular Coulombic decay (ICD) [19, 20], a process which occurs when a laser pulse removes a core electron from an atom or molecule in a dimer. An outer electron of the same atom can fill the hole left by the core electron. The excess energy is transferred to the neighboring atom, causing the ejection of an outer electron from this neighboring atom. In Chapter 4, we will show another decay process which also becomes more effective in a van der Waals system.

Cooling molecules or atoms further eventually creates solid matter. Properties of a solid not only depend on the species of the atoms, but arise from the arrangement of the atoms. For example, graphite and diamond are both solid forms of carbon, but are obviously different in color, hardness, conductivity, and many other properties.

Energy bands and a bandgap emerge from the coupling among many atoms. The bandgap plays the same role as ionization potential in atoms or molecules. The coupling also reduces the threshold for electron-hole pair generation, providing an opportunity for generating high-order harmonics at high repetition rates needed for frequency combs [21]. Atoms in a solid have fixed positions relative to each other, which allows fixed symmetry properties. By choosing material with the right symmetry, one can generate even order harmonics, or elliptically polarized harmonics [22]. Moreover, fabrication with solid materials is very advanced. On one hand, this allows researchers to investigate solid systems under different conditions, such as doping the material [23], or under the impact of a DC field [24]. On the other hand, it opens up opportunities for new technology in attosecond electronics and chemical imaging.

The thesis is organized as follows:

- In Chapter 2, I introduce the experimental techniques used for measuring molecules.

- In Chapter 3, we study the photodissociation process of NO_2. A 400 nm photon excites NO_2 through an electronic transition. Then a strong laser pulse ionizes the molecule for detection. The molecule undergoes internal vibrational energy redistribution before it dissociates.
- In Chapter 4, we investigate the dissociation process of CO^{2+} in a $(CO)_2$ dimer, using a laser pulse to remove three electrons from $(CO)_2$. Compared to a monomer, the CO^{2+} in the dimer has a new dissociation pathway, which is both prompt and produces fragments with higher kinetic energy. This new pathway arises from coupling of different charge states in the dimer complex.
- In Chapter 5, we generate up to the 7th harmonic in silicon and zinc oxide with femtosecond pulses from a thulium fiber laser at a repetition rate of 93 MHz. We observe thermal effects but no material damage. This experiment demonstrated the potential to generate frequency combs at short wavelengths using harmonics generated in a solid.

Chapter 2

Measuring molecules

The NO_2 experiments in Chapter 3 and $(CO)_2$ experiments in Chapter 4 were performed using a COLd Target Recoil Ion Momentum Spectrometer (COLTRIMS). Key points of the apparatus and the laser system are briefly described in this chapter. More details about COLTRIMS can be found in [25, 26, 27]. Details about solids experiments are in Chapter 5.

2.1 COLTRIMS

In COLTRIMS, we ionize a molecule with a strong laser pulse. For each resulting electron and ion, we measure its time-of-flight (TOF) and position on the detector, and infer the three dimensional momentum.

Our COLTRIMS consists of three vacuum chambers: a source chamber, a collimator chamber and a main chamber, shown in Fig. 2.1 (a). The source chamber provides the molecular beam for experiments. Molecules are cooled by expanding gases into vacuum through a 10 μm nozzle. A skimmer between the source chamber and the collimator chamber selects the central coldest part of the molecular beam. The collimator chamber selects the most collimated part of the molecular beam with a 1 mm aperture before the beam goes into the main chamber. Before the aperture, a piezoelectric slit with a maximum width of 350 μm (Piezosystem Jena PZS4V, Ser.No. 95246) makes the molecular beam even narrower. The main chamber contains the spectrometer. Molecules interact with the laser in the main chamber.

The chambers are differentially pumped. The pressure of the source chamber is below 10^{-3} mbar while the background pressure for the main chamber is at 10^{-10} mbar.

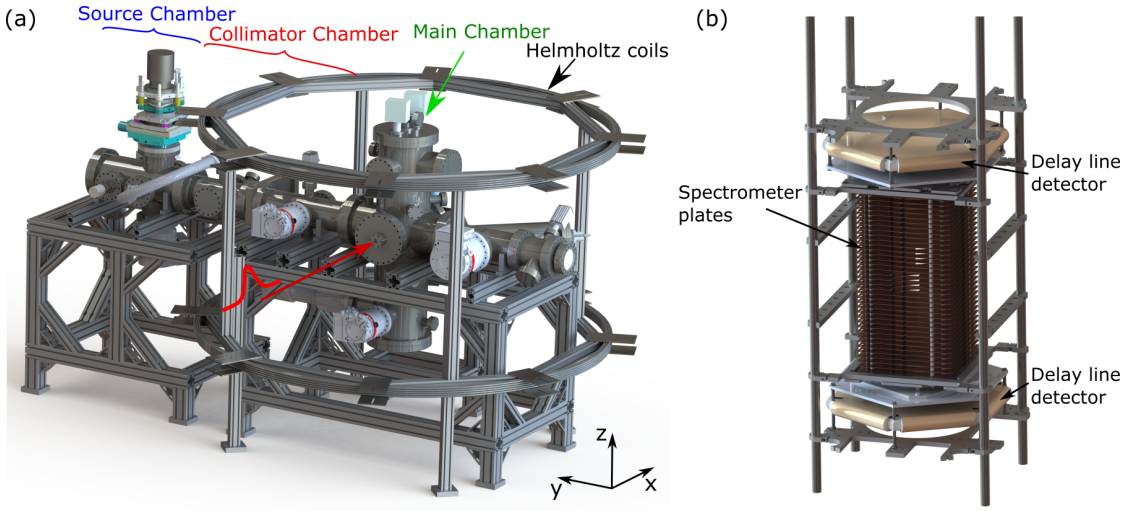

Figure 2.1: (a) The COLTRIMS apparatus in JASLab. The molecules go into the chamber from the left. The red arrow shows the direction of the laser. The laser beam is focused with a parabolic mirror (f = 50 mm). (b) Spectrometer.

In the spectrometer, a set of copper plates spatially separated by a few millimeters is connected with strong resistors, providing a homogeneous static electric field to guide the charged particles onto the detectors at the two ends, see Fig 2.1(b). The total length of the spectrometer is 20 cm. A 50 mm focal length parabolic mirror resides within the spectrometer plates to focus the laser onto the molecular beam. The electrons and ions are born in the middle, 10 cm away from each detector.

When an atom is singly ionized, the electron momentum and the ion momentum are equal in magnitude. Since electrons have a much smaller mass than ions, their velocities are much higher. As a result, electrons tend to fall out of the detector surface. To avoid this problem, we apply a homogeneous magnetic field parallel to the spectrometer using the Helmholtz coils. The magnetic field forces the electrons to rotate in a helical motion, confining them along the spectrometer axis so they will land on the detector.

Both electron and ion detectors consist of a microchannel plate (MCP, Roentdek Zstackset75) and a delay line detector (Roentdek Hex90 for the electron detector and Roentdek Hex75 for the ion detector). When an electron or ion arrives at the MCP, it triggers an electron cascade. The electron avalanche is picked up by the delay line detector behind the MCP.

The delay line detector measures the position of the fragments. Both delay line detectors in our apparatus consist of three wires at 60 degrees to each other. Each wire

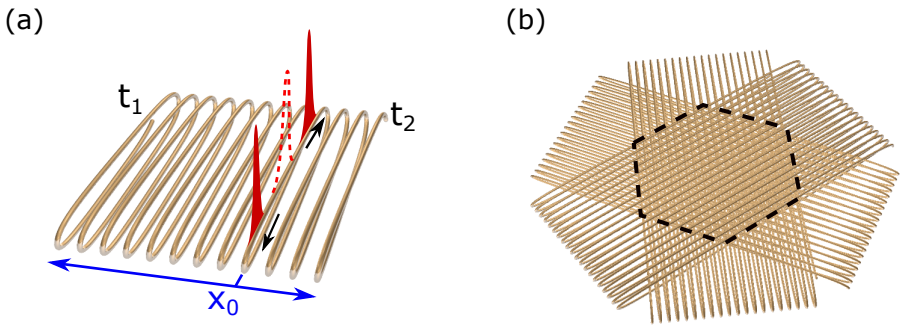

Figure 2.2: (a) Sketch of a single delay line. When an electron pulse (dashed red) from the MCP hits the delay line, it gives rise to two current pulses propagating towards the two ends (solid red). The arrival times at the two end, t_1 and t_2, are measured. The difference between the arrival times gives the position along the wire, and thus the position of the hit in the direction perpendicular to the wire (x_0 along the blue arrow). (b) Three delay lines at an angle of 60 degrees to each other make a hexagonal detection surface (area within the black dashed lines).

loops many times to make a detection surface, shown in Fig. 2.2(a). When a burst of electrons from the MCP hits the delay line, the electrons create two current pulses that propagate in both directions at a constant speed. The arrival time at each end is measured. The difference between the arrival times gives the position along the wire. With the size of the loops known, we then obtain the position of the hit in the direction perpendicular to the wire in the loops (see the blue arrow in Fig. 2.2(a)). Three delay lines make a hexagonal detection surface, shown in Fig. 2.2(b). Two delay line anodes can measure the position of a fragment, and having an additional layer reduces the dead-time between particle hits and improves multihit readout [28].

2.1.1 Jet temperature estimation

The molecular beam is cooled by expanding high pressure gases through a 10 μm nozzle into a vacuum. This process lowers not only the translational temperature, but also the vibrational and rotational temperature of the molecules. In the directions perpendicular to the molecular beam, x and z, a skimmer and an aperture further decreases the translational temperature by only letting the central part of the molecule beam, which has the smallest transverse velocities and thus lowest temperatures, into the detector chamber. We neglect the thermal spread in the transverse directions, and estimate the temperature of the molecules using their momentum distribution.

The momentum distribution of molecules at temperature T in one dimension can be described with the Maxwell Boltzmann distribution:

$$f_p = \frac{1}{2\pi m k_B T} \exp(-\frac{p^2}{2mk_BT}) \tag{2.1}$$

where $p = p_{ion} + p_{elec}$ is the molecular momentum along the jet direction. The momentum has a Gaussian distribution with variance

$$\sigma^2_{therm} = mk_BT \tag{2.2}$$

Experimentally, both the thermal distribution and detector resolution contribute to the variance, $\sigma^2_{meas,y} = \sigma^2_{spec,y} + \sigma^2_{therm,y}$. The momentum along x and y are both measured with the delay line detectors, and thus have the same variance, $\sigma_{spec,y} = \sigma_{spec,x}$. Considering that the thermal spread along x is negligible, $\sigma_{spec,x} \gg \sigma_{therm,x}$, we have

$$mk_bT = \sigma^2_{therm,y} \approx \sigma^2_{meas,y} - \sigma^2_{meas,x} \tag{2.3}$$

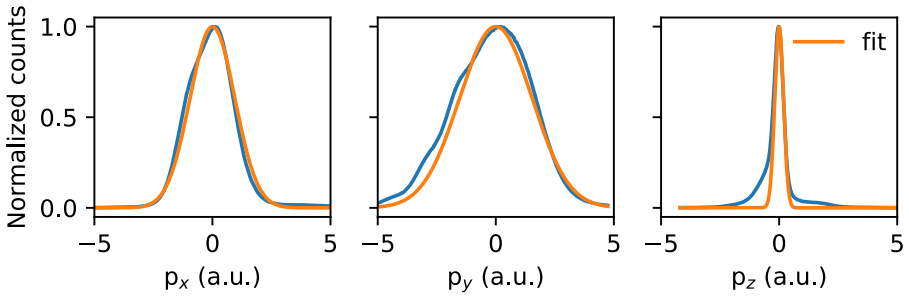

Figure 2.3: Sum momentum of CO^+ and an electron in coincidence. Blue curves are experimental results and orange curves are fitting results. $\sigma_{meas,x} = 1.34$ atomic units (a.u.), $\sigma_{meas,y} = 2.17$ a.u., $\sigma_{meas,z} = 0.26$ a.u..

Figure 2.3 shows the sum momentum of CO^+ and an electron in coincidence. We obtain the temperature of the CO molecules:

$$T = (\sigma^2_{meas,y} - \sigma^2_{meas,x})/mk_b = 17.7K \tag{2.4}$$

2.1.2 Assigning properties to fragments

For each fragment, the detector returns its position and time-of-flight (TOF). Undissociative molecular ions, which are created by removing one electron from a neutral molecule, have a small momentum along the time-of-flight direction. Their momentum

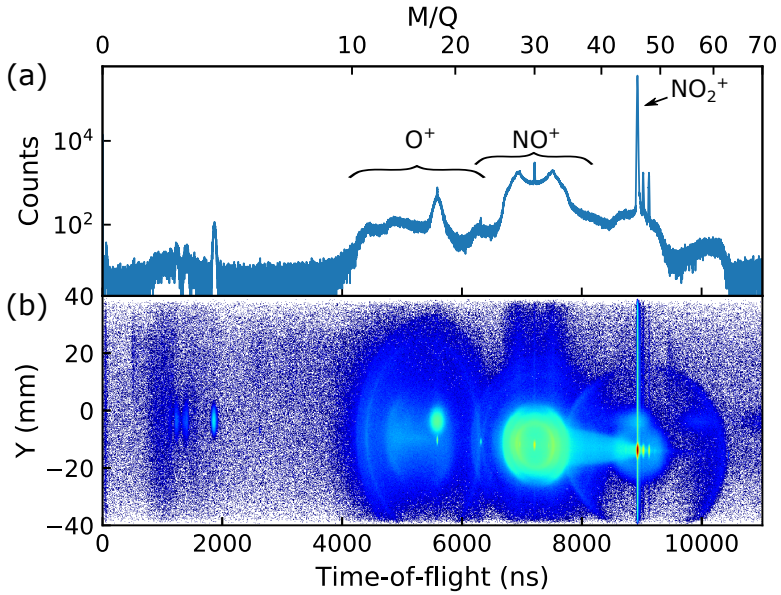

Figure 2.4: Time-of-flight spectrum. The top axis shows the mass-to-charge ratio assuming all fragments start stationary. The NO_2^+ molecular ions have small initial velocity, and thus a narrow peak in the spectrum. The NO^+, which is a fragment ion from breaking up a NO_2 molecule, covers a much larger range in time-of-flight.

distribution is broadened only by the thermal distribution and the recoil from the photoelectron. Therefore, these ions exhibit only a small spread in their time-of-flight and appear as narrow peaks. The peak position is directly proportional to the square root of the molecular mass M and charge Q ratio, $TOF \propto \sqrt{M/Q}$. If an ion originates from a Coulomb explosion event, the fragment often has a large momentum. Large momentum along the time-of-flight will result in broad, and possibly multiple peaks in the spectrum. The broad time-of-flight from ion species with different mass-to-charge ratios can overlap, and identifying these ions is less straightforward. For the dissociation channels that overlap in the time-of-flight, we first assign one possible mass-over-charge to a fragment and then test the assignment by checking if another fragment in the same event comes from the same molecule. If the two fragments have a small sum momentum, the assignment is good and the fragments come from the same molecule. If the sum momentum of the two tentatively assigned fragments is larger than a predetermined value (usually around 10 a.u.), we discard the event.

An ionization event producing more than one fragment ion carries information such as molecular geometry and molecular orientation. Such events can be easily identified on a photoion-photoion correlation map (PIPICO). PIPICO for two particles is a 2D histogram with the time-of-flight of the first ion on one axis, and time-of-flight of the

second ion on the other axis, see Fig. 2.5. The first or second are determined by the order of their arrival on the detector.

When a molecule breaks up into two fragment ions, the two fragments will have opposite momentum. If one fragment has momentum towards the ion detector, the other fragment will fly away from the detector. Compared to stationary fragments with the same mass-to-charge ratio, each fragment will have either a smaller or larger time-of-flight. Therefore, a two-particle breakup channel will show up as a curve on the correlation map, for example, the NO^++O^+ from a NO_2 molecule in Fig. 2.5. Similarly, a breakup with three particles can be identified by plotting a correlation map between the time-of-flight sum of two particles and the time-of-flight of the third particle. Sometimes we also observe horizontal or vertical lines in the correlation map. These arise from detecting any fragment in the same laser shot as a molecular ion, which has a narrow time-of-flight.

Since the molecules from the jet have very small momentum, the sum momentum of fragments from the same molecule is also small due to momentum conservation. Therefore we can identify fragments from the same molecule by checking their sum momentum. However, if the fragments have small momenta, for example molecular ions, they may come from different molecules but still have a small sum momentum. Therefore, we also require the momentum of each fragment to be large to guarantee that they come from the same molecule.

If multiple fragments are detected in the same laser shot, we say these fragments are in coincidence, and if they are also from the same molecule, we call them "correlated". If the fragments come from the same laser shot but not from the same molecule, they are a "false coincidence". We keep the gas pressure low so that, most of the time, at most one molecule is ionized in each laser shot. However, false coincidences still exist, such as the horizontal line in Fig. 2.5. Therefore, it is necessary to check the sum momentum for each multi-hit event.

2.2 Laser

We use a Ti:Sapphire laser system (Coherent Legend Elite Cryo) for the COLTRIMS experiments. The laser system is seeded by a Ti:Sapphire oscillator (Coherent Micra), which provides 800 nm, 20 fs, 1 nJ pulses at about 80 MHz. The pulses are amplified in two stages. The first stage (Coherent Elite Duo) includes a stretcher, a regenerative amplifier (Regen), and a single pass amplifier (SPA). This stage is pumped by an Evolution HE 75 system, which outputs 532 nm pulses at 10 kHz, with a power of 50 W. The Regen and SPA are each pumped by 25 W. Pulses out of this stage amplification are 1.1 mJ at 10 kHz with a picosecond pulse duration. The second stage (Coherent Cryo) contains a

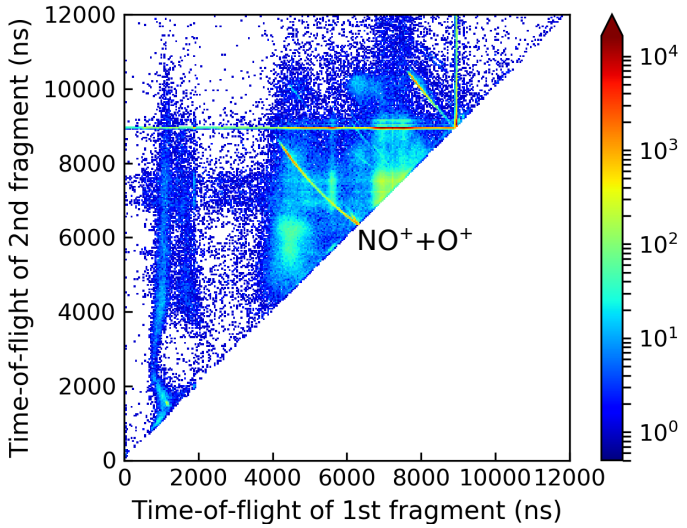

Figure 2.5: Photoion photoion correlation map. Each pixel corresponds to an event with 2 fragments. The curves on the map indicate two-fragment breakups. For example, the $NO_2^{2+} \rightarrow NO^+ + O^+$ are shown in the plot. The horizontal and vertical lines show false coincidences where ions with various mass-to-charge ratios are detected in the same laser shots as NO_2^+.

single pass amplifier with the Ti:Sapphire crystal in vacuum (1×10^{-8} Torr) and cooled to 80 K by cryogenic cooling. This stage is pumped by another identical Evolution HE 75 system. After the two stages, we get 800 nm, 25 fs, at a 10 kHz repetition rate, with a pulse energy of 1.6 mJ. About 15% of the beam is sent to the COLTRIMS setup. In the COLTRIMS chamber, the laser pulses are focused into the molecular beam with a 50 mm focal length parabolic mirror.

2.2.1 Intensity estimation

We calibrate the laser intensity by measuring the drift momentum of the electron formed by ionizing an atom/molecule by a circularly polarized laser pulse [29]. The drift momentum in the polarization plane is $p_d = qE(t_i)/\omega$, where q is the charge of the particle, $E(t_i)$ is the electric field of the laser pulse at the time of ionization t_i, and ω is the laser frequency. The intensity of the circularly polarized pulse is $I_0 = c\epsilon E_0^2$, where E_0 is the electric field at the peak of the laser pulse. We assume most of the ionization occurs at the peak field, $E(t_i) = E_0$. From this, we can obtain a peak laser intensity $I_0 = c\epsilon(p_d\omega/q)^2$.

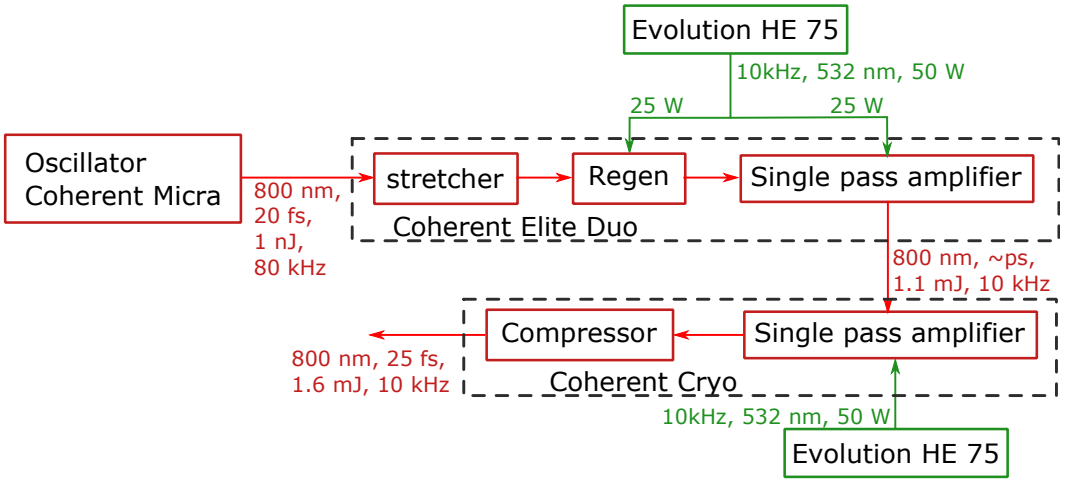

Figure 2.6: Illustration of the Ti:Sapphire system.

2.2.2 Overlapping two pulses at different wavelengths

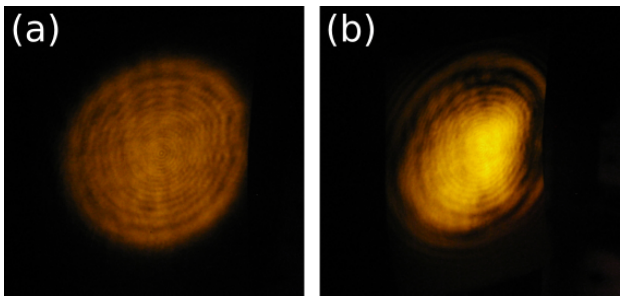

Figure 2.7: Profile of the 400 nm pulse when it comes (a) before and (b) after the 800 nm pulse. The plasma generated by the intense 800 nm pulse modifies the profile of the 400 nm beam.

In the NO_2 experiments, we use a 400 nm pulse as the pump and an 800 nm pulse as the probe. We first overlap the two beams spatially. To find the temporal overlap, we focus them outside the chamber with a 50 mm focal length mirror, and look at the beam profile of the 400 nm on a white card a few centimeters after the focus. The 800 nm pulse is not visible through laser goggles. We keep the 800 nm beam strong enough to create plasma but not generate much supercontinuum to overwhelm the profile of the 400 nm beam. If the 400 nm pulse comes after the 800 nm, the generated plasma modifies the refractive index, and thereby changes the beam profile of the 400 nm beam. Otherwise, if the 400 nm pulse comes before the 800 nm, the beam profile of the 400 nm remains unchanged. Since the plasma lifetime is relatively long, this method provides a clear

binary diagnosis for temporal overlap, and therefore is easy for finding the rough overlap in experiments.

The temporal overlap may change slightly when both beams are sent into the COLTRIMS chamber. We do a cross-correlation in the chamber by checking the ionization rate to find the more accurate in-chamber temporal overlap.

Chapter 3

Dissociation of NO_2

3.1 Photoexcitation of NO_2

Nitrogen dioxide plays an important role in atmospheric chemistry, particularly air pollution. One major source of NO_2 is combustion in automobiles and power plants. NO_2, together with other oxides of nitrogen, participates in a series of reactions for formation of nitric acid which contributes to acid rain. Photodissociation of NO_2, $NO_2 + h\nu \rightarrow NO + O$, provides an oxygen atom that can combine with an O_2 molecule to form ozone at ground level [30, 31], which is a major component in smog. The photodynamics of NO_2 are complex, even though it is made of only three atoms. NO_2 has one unpaired electron and this open-shell electronic structure gives rise to highly coupled electronic states, leading to rich photodynamics features usually occurring in much larger molecules [32]. This provides an opportunity for studying complex phenomena in a smaller molecule.

In the ground electronic state, $\tilde{X}^2A_1$, NO_2 has a bent geometry with a bond angle of 134 degrees, and the dominant electronic configuration is $(b_2)^2(a_1)^1$. Single photon absorption at 400 nm excites NO_2 to its $\tilde{A}^2B_2$ state, with a dominant electronic configuration of $(b_2)^1(a_1)^2$ (see Fig. 3.1 (a)). The $\tilde{A}^2B_2$ state forms a conical intersection with the ground electronic state. After photoexcitation, the nuclear wavepacket moves along the bending coordinate towards the conical intersection where some population can return to the ground electronic state, shown in Fig. 3.1 (c). Most of the population returns to the ground electronic state within a few hundred femtoseconds [8, 33].

If the photon energy is above the dissociation threshold at 3.1155 eV [35] (397.95 nm), the NO_2 molecule can dissociate into NO and O fragments [32]. In order to dissociate, the vibrational energy that is initially in the bending mode has to be coupled to asymmetric stretching. The dissociation process has been described statistically, where the

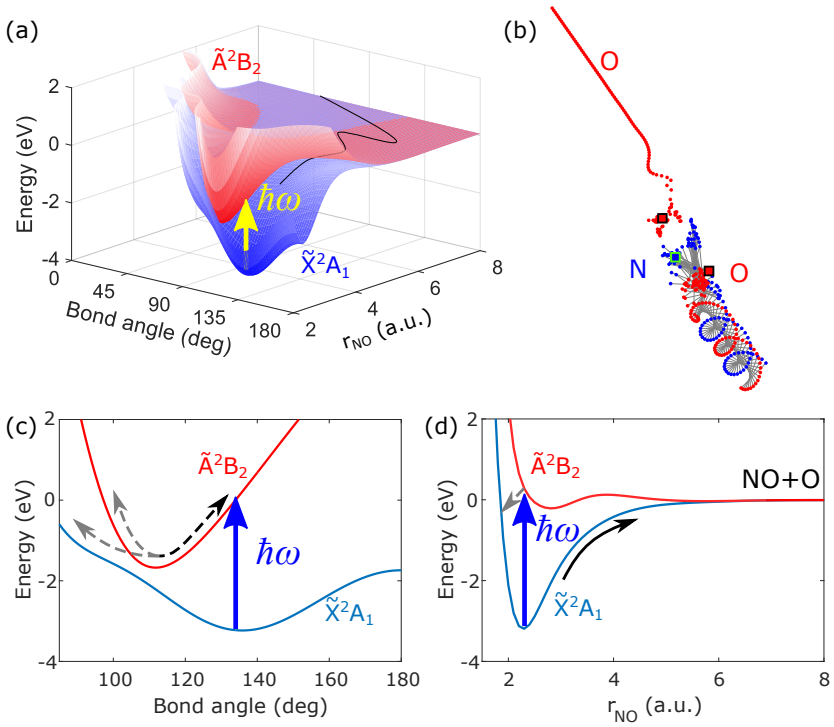

Figure 3.1: (a) Potential energy surface of the ground (shown in blue) and the first excited (shown in red) electronic state as a function of bond angle and one bond length [34]. The other bond length is fixed at 2.26 a.u.. The asymptotic energy of the ground electronic state is at zero. (c) and (d) are one dimensional potential energy surfaces. Single photon absorption can excite the molecule to the $\tilde{A}^2B_2$ state. The wavepacket crosses the conical intersection several times, shown in dashed arrows in (c). After about 200 fs, the population transfers back to the ground electronic state $\tilde{X}^2A_1$. If the excitation photon energy is higher than threshold (3.115 eV), the molecule can dissociate on the ground electronic state, shown in black curves in (a) and (d). (b) shows a simulated trajectory of NO_2 dissociation. The blue and red dots show the position of the nitrogen and the two oxygen atoms in the dissociation. The squares show the initial positions of the atoms. The molecule undergoes complex motions before the NO-O bond significantly stretches. The molecule eventually dissociates into NO and O, and the NO fragment spins as the NO-O distance increases.

intramolecular vibrational energy is assumed to randomly redistribute instantaneously [36]. Early experiments mostly measured the final products [37, 38, 39]. Time-resolved studies using femtosecond lasers have been carried out to investigate dynamics originating

from the $\tilde{A}^2B_2$ state [40, 41]. Recently, high harmonic generation [8] and photoelectron spectroscopy [11] have attempted to access the underlying electronic and nuclear dynamics by mapping the electronic state evolution. Here, we directly follow the nuclear dynamics of NO_2 on the ground electronic state using photoion-photoelectron momentum imaging.

The NO_2 photodissociation dynamics induced by a single 400 nm photon can be contaminated by multiphoton processes [32]. An oscillation in the high harmonic signal from the early dynamics of the dissociating molecule was attributed to electronic dynamics around the conical intersection between $\tilde{A}^2B_2$ and $\tilde{X}^2A_1$ [8]. Subsequent experiments showed that the form of the peaks in the oscillations depended differently on the pump intensity. This confirmed that the different maxima seen in the pump-probe data are not wavepacket dynamics on a single state but rather due to multiphoton processes [11]. We observe multiple channels in our experiments. The major channel is from excitation by a single 400 nm photon. Multiphoton excitation exists, but those channels are weak.

3.2 Classical trajectory simulation

We simulated NO_2 dissociation on the ground electronic state classically. The simulation is done in Jacobi coordinates, see Fig. 3.2. The classical Hamiltonian for this system is:

$$H = E_R + E_r + E_{rot} + V(R, r, \gamma) \tag{3.1}$$

with

$$\begin{aligned} E_R &= P_R^2/(2m_R), \\ E_r &= P_r^2/(2m_r), \\ E_{rot} &= B(R, r)P_{rot}^2 \end{aligned}$$

where R is the distance between O and center of mass NO, r is the NO bond length, γ is the angle between R and r. Figure 3.2 shows the coordinates. $m_R = m_{NO}m_O/(m_{NO} + m_O)$ and $m_r = m_N m_O/(m_N + m_O)$ are the reduced mass for the O-NO and NO respectively. $B(R, r) = 1/2m_R R^2 + 1/2m_r r^2$ is the coordinate dependent rotational constant. P_R, P_r, and P_{rot} are the momenta corresponding to stretching of R, r and rotation. $V(R, r, \gamma)$ is the potential energy surface of the ground electronic state X^2A_1 state. We use an analytical potential energy surface by Reignier *et al.* in the simulation [34].

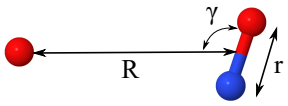

Figure 3.2: Geometry of NO_2. The O atoms are in red and the N atom is in blue.

In Hamiltonian mechanics,

$$\frac{\partial H}{\partial q^j} = -\dot{p}_j, \frac{\partial H}{\partial p_j} = \dot{q}^j \tag{3.2}$$

Apply equation 3.2 to 3.1, we get

$$\begin{cases} \dot{R} = \dfrac{P_R}{m_R} \\ \dot{r} = \dfrac{P_r}{m_r} \\ \dot{\gamma} = 2B(R,r)P_{rot} \\ \dot{P_R} = -\dfrac{\partial B(R,r)}{\partial R}P_{rot}^2 - \dfrac{\partial V(R,r,\gamma)}{\partial R} \\ \dot{P_r} = -\dfrac{\partial B(R,r)}{\partial r}P_{rot}^2 - \dfrac{\partial V(R,r,\gamma)}{\partial r} \\ \dot{P_{rot}} = -\dfrac{\partial V(R,r,\gamma)}{\partial \gamma} \end{cases} \tag{3.3}$$

We use a 5th order Runge-Kutta method for solving the equations of motion. To be consistent with the experiment, we use single photon excitation by a 400 nm pulse with a 5 nm bandwidth. The distribution of initial geometry is chosen based on the wavepacket

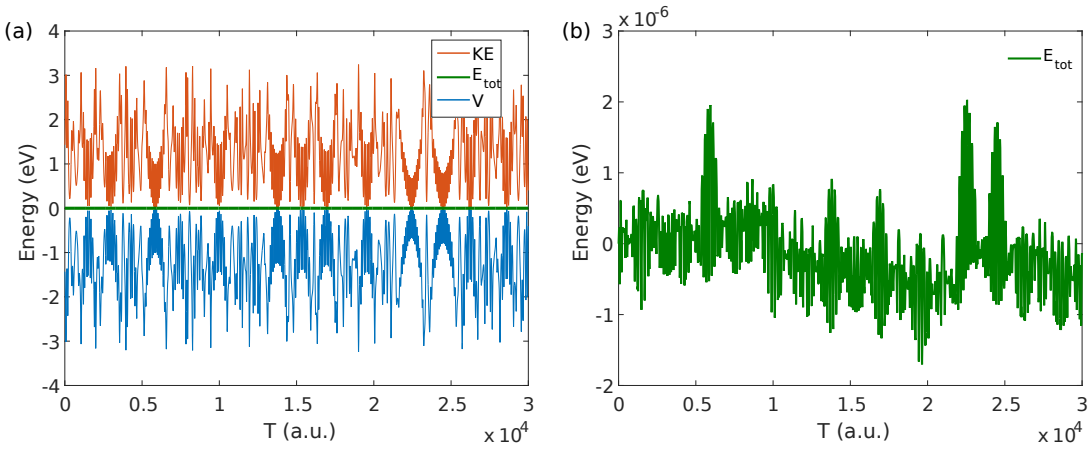

Figure 3.3: Energy conservation of the trajectory simulation. The blue line is the potential energy of the molecule; the red line is the kinetic energy of the particles; the green line is total energy of the system. (b) is a zoom of the total energy from (a). The total energy is conserved on the order of 10^{-6} eV.

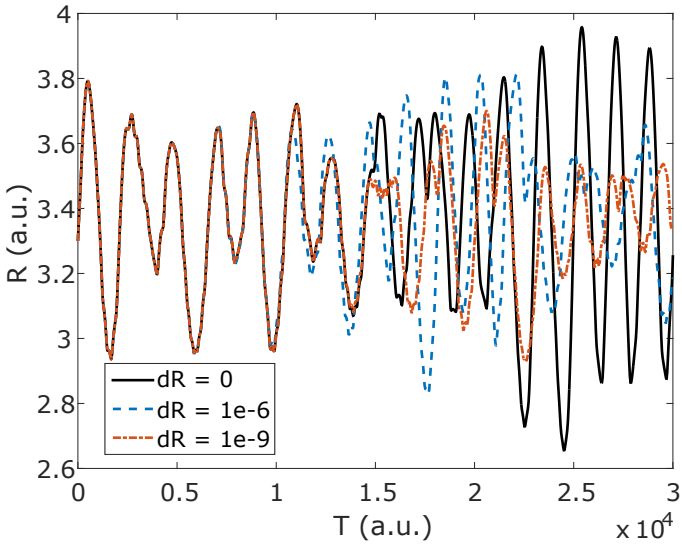

Figure 3.4: NO_2 trajectories with slightly different initial conditions. Initial parameter $R = R_0 + dR$, where $R_0 = 3.3$ a.u., and $dR = 0$, 10^{-6}, and 10^{-9} a. u., respectively. All other parameters are kept the same.

calculated by Arasaki *et al.* [33]. The initial N-O bond lengths are 1.25 ± 0.1 Å and 1.43 ± 0.1 Å, and the bond angle is 130 ± 30 degrees. Each geometry parameter follows a uniform distribution. The bond lengths and bond angles are converted to the coordinate shown in Fig. 3.2. The kinetic energy is shared randomly among E_R, E_r, and E_{rot}. With such initial conditions, we predict the evolution of the molecular geometry for 3 ps by propagating the particles classically.

One crucial check of the integration is the test for energy conservation. Figure 3.3 shows the energy conservation in the trajectory simulation. As the fragments propagate, we observe the exchange of energy between potential and kinetic energy, while the total energy is conserved to the order of 10^{-6} eV.

When we change the initial conditions of the simulation by a small amount, the trajectory becomes very different at a long propagation time. In Fig. 3.4, we plot three trajectories with similar initial conditions. The O-NO distance, R, starts at 3.3 a.u., and is modified by 10^{-6} and 10^{-9} a.u., while all other initial parameters are kept the same. The three trajectories become significantly different after $T = 1.5 \times 10^4$ a.u. (363 fs). This suggests that the system is chaotic, meaning that small inaccuracy in initial conditions will result in completely different trajectories. However, we can still explore the possible geometry for a large ensemble of molecules.

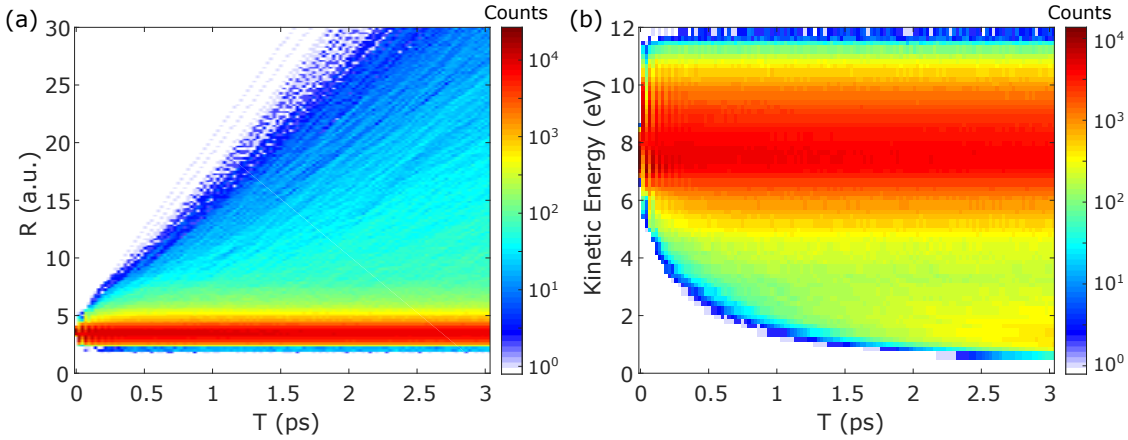

Figure 3.5: (a) Simulated results of distribution of NO-O distance as a function of propagation time. (b) Kinetic energy release of the fragment ions, assuming all the molecules in the simulation break into NO^++O^+, and the fragments only repel each other via Coulomb interactions.

In Fig. 3.5 (a), we plot the NO-O distance as a function of propagation time. We use $1/R$ to convert the distance into kinetic energy release and plot it in Fig. 3.5 (b). Since the central wavelength of the excitation pulse is below excitation threshold, most molecules are vibrationally excited but do not dissociate. Molecules that can eventually dissociate also spend a long time exploring many geometries. Overall, the dissociation is a delayed process.

3.3 Experiments

The experiments were performed in COLTRIMS [25, 10] (see section 2.1 for details). Presented in Fig. 3.6 is a schematic diagram of the experimental setup. We mixed 5% of NO_2 in helium and expanded it through a 30 μm nozzle at a backing pressure of 1 bar. The nozzle was heated to 80 °C to reduce the NO_2 dimer concentration. We estimated that the NO_2 translational temperature along the jet was 105 K, based on the molecular momentum distribution (see section 2.1.1 for details).

We use a pump-probe scheme in the experiments. Our Ti:Sapphire laser system (Coherent Legend Elite Cryo) delivers 800 nm, 25 fs pulses at 10 kHz repetition rate. The beam was split into two: one beam was frequency doubled in a 300 μm thick BBO crystal, serving as the pump; the probe 800 nm beam was used for strong field ionization. The temporal overlap between the 400 nm pump and 800 nm probe pulses was determined by evaluating the non-resonant ionization of H_2. Cross correlation between the 800 nm

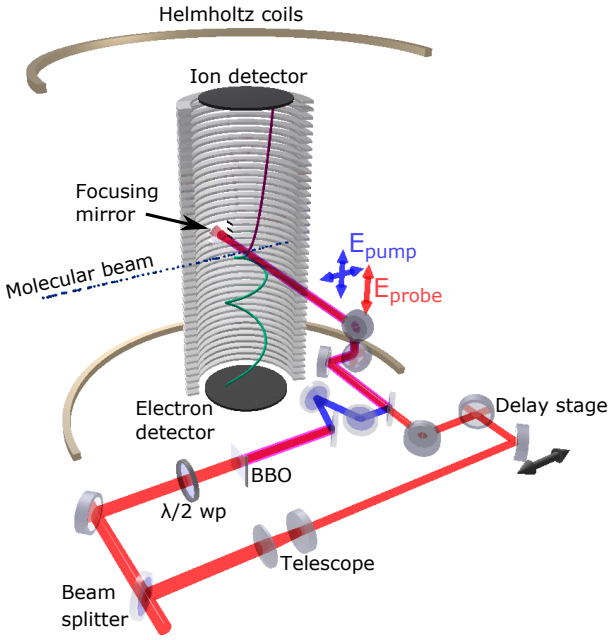

Figure 3.6: Sketch of the experimental setup. A $\lambda/2$ waveplate is used to control the pump pulse polarization. The first 4 mirrors after the BBO crystal are dichroic mirrors that transmit 800 nm and reflect 400 nm. They remove the 800 nm pulse from the pump beam and the last one combines the pump and probe beams.

and 400 nm provided an approximate pulse duration of 56 fs for the 400 nm pump pulse. The pump pulse has a central wavelength of 400 nm and 5 nm bandwidth at full width half maximum (FWHM). The polarization of the probe pulse is along the time-of-flight axis, whereas the polarization of the pump pulse is either parallel or perpendicular to the probe (see Fig. 3.6). Both pulses are focused into the molecular beam with a parabolic mirror (f = 50 mm).

We estimate the probe pulse intensity by measuring the ion momentum of H_2^+ ionized by a circularly polarized pulse. In section 3.4 and 3.5, the peak intensity at the laser focus is estimated to be 2.4×10^{12} W/cm^2 and 1.2×10^{14} W/cm^2, for the pump and probe pulse, respectively. No ionization events were observed with the pump pulse alone. For each polarization geometry, we performed two experiments: one scans the pump-probe delay from -0.2 ps to 1 ps, with a step size of 20 fs; the other collects data at a few individual delays for better statistics. In section 3.6, we use the same pump but a stronger probe with an intensity of 1.8×10^{15} W/cm^2, and scan the pump-probe delay from -100 fs to 300 fs with a step size of 10 fs.

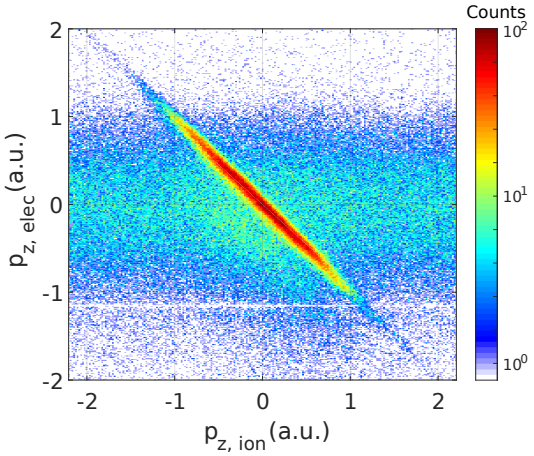

Figure 3.7: NO^+ and electron correlation measured with the 800 nm pulse only. On the bright line, the NO^+ and electron have opposite momenta with the same magnitude, indicating that they originate from neutral NO molecules.

In our results, we observe some NO^+ and electron in coincidence even without the 400 nm pump pulse. Figure 3.7 shows the momentum of these fragments along the time-of-flight axis. Fragments on the bright line in the figure have opposite momentum with the same magnitude, and therefore originate from ionization of neutral NO molecules. We estimated the amount of NO using the ratio of two channels: $NO \rightarrow NO^+ + e^-$ and $NO_2^+ \rightarrow NO_2^+ + e^-$, and found that there were about 0.03% free NO contamination in the NO_2 gas mixture. Signals from the NO molecules do not depend on pump-probe delay. In the following results, these events are removed from the data by subtracting signals at negative delays, i.e., when the probe precedes the pump. Other time-independent signals, such as dissociative ionization of NO_2 by the 800 nm pulse only, are therefore also removed by the subtraction.

3.4 Probing with single ionization

First we study the single ionization channel $NO_2 \rightarrow (NO_2)^* \rightarrow NO^+ + O + e$. For this channel we detect the NO^+ and the electron. The momentum of the neutral oxygen atom is obtained via momentum conservation. Figure 3.8(a) shows the total kinetic energy release (KER) as a function of delay. Results with parallel and perpendicular pump-probe polarizations are very similar, so we only show results for parallel polarization. We analyze the kinetic energy spectrum in three regions: $0 - 0.6$ eV, $0.6 - 1.8$ eV and $1.8 - 3.5$ eV. Figure 3.8(b) shows the kinetic energy integrated over pump probe delays

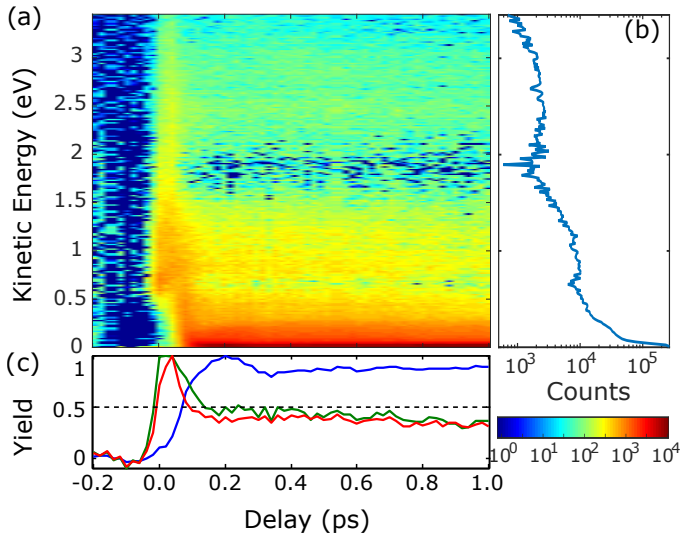

Figure 3.8: (a) Time-resolved total kinetic energy release of the channel $NO_2 \rightarrow (NO_2)^* \rightarrow NO^+ + O + e$. The background has been subtracted. (b) Kinetic energy release integrated from 0.4 ps to 1 ps. (c) Time resolved, normalized ion yield of NO^+ with different total kinetic energy release: blue curve, 0-0.6 eV; green curve, 0.6-1.8 eV; and red curve, 1.8-3.5 eV. The black dashed line is yield = 0.5, as a guide for the eye.

from 400 fs to 1 ps. The three peaks in Fig. 3.8(b) correspond to the three energy regions. Figure 3.8(c) shows the time dependent ion yield of the three regions. For the low energy region (0 – 0.6 eV, blue line), the signal exhibits a peak at about 0.2 ps, then a local minimum at about 0.35 ps followed by a slow increase. The higher energy regions (green and red lines) show a peak at earlier delay and then a slow decrease.

The low energy channel agrees well with the single photon excitation results by Forbes *et al.* [11]. At 200 fs, most of the excited population returns to the ground electronic state. Near the conical intersection, at a bond angle of 102 degrees, the ionization rate on the ground electronic state has a local maximum [8]. Therefore, the ion yield has a peak at 200 fs. At a long pump probe delay, more NO fragments are produced from the NO_2 dissociation. Since the ionization potential of NO (9.26 eV) is slightly lower than NO_2 (9.58 eV), ion yield slowly increases at long pump-probe delays.

In Fig. 3.9(a) we show the sum momentum of NO^+ and the electron in coincidence along the time-of-flight direction, $p_{z,sum} = p_{z,e} + p_{z,NO^+}$, for the low energy channel. We observe the peaks around 0.2 ps and the slow increase of the signal at long delay. At 0.2 ps, the sum momentum distribution exhibits a double peak structure, with few events at $p_{z,sum} = 0$ a.u.. From 300 fs to 1 ps, the two peaks gradually merge into a single peak centered at 0 a.u.. This feature is shown more clearly in Fig. 3.9(b), where the sum

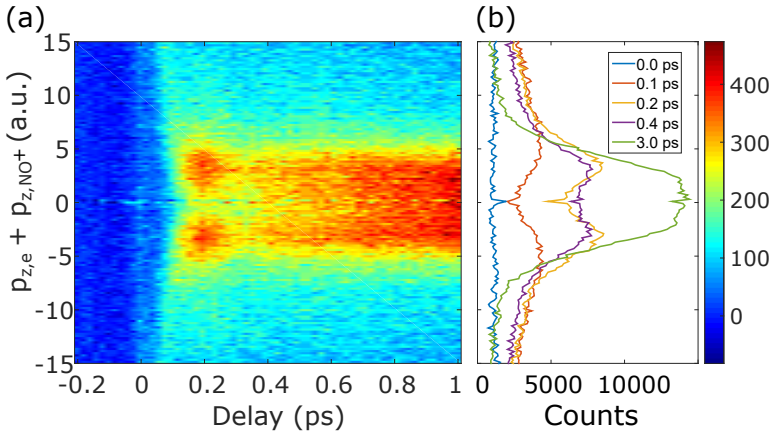

Figure 3.9: (a) Sum momentum of NO^+ ion and an electron in coincidence. (b) Sum momentum distribution for individual delays. As delay increases, the number of fragments with zero momentum increases, indicating an increasing number of dissociation product NO.

momentum distribution is plotted for individual delays.

The non-zero momentum at early pump-probe delay indicate that in the creation of $NO^+ + e^-$, the oxygen atom provides a recoil. Therefore, the NO-O distance must be small. The small NO_2 molecules are first ionized and then dissociate into NO^+ and O fragments. At long delay, some NO^+ and electrons have zero sum momentum, just like the ionization of free NO molecules, where no recoil from another particle is involved. This indicates that the NO-O distance in these events are large and the effect of the O atom on NO is small.

Since our excitation pulse has most of the spectrum below the dissociation threshold, many of the excited NO_2 molecules are at high rovibrational levels on the ground electronic state but do not dissociate. Thus, at long delays, the probe pulse will ionize an ensemble of dissociating/dissociated molecules and highly excited but bound molecules. These two subsets cannot be separated clearly in the single photon excitation case. We will discuss more about the dissociated molecules in the double ionization channel.

In Fig. 3.10 we plot the angular distribution of the NO^+ momentum in the laboratory frame. The pump and probe polarizations are parallel for Fig. 3.10(a) and (b), and perpendicular for Fig. 3.10(c) and (d). For both polarization geometries, the probe polarization remains along the time-of-flight direction and the pump polarization is rotated by 90 degrees. The polarizations are shown on the left inserts in the figure. Fig. 3.10(a) and (c) show the angular distribution of the NO^+ with the lowest kinetic energy (KER $<$ 0.06 eV, or $|p_{z,sum}| < 9$ a.u.). At short pump-probe delay, we observe distinct anisotropic features: a two-lobe structure primarily along polarization for the parallel case, and a

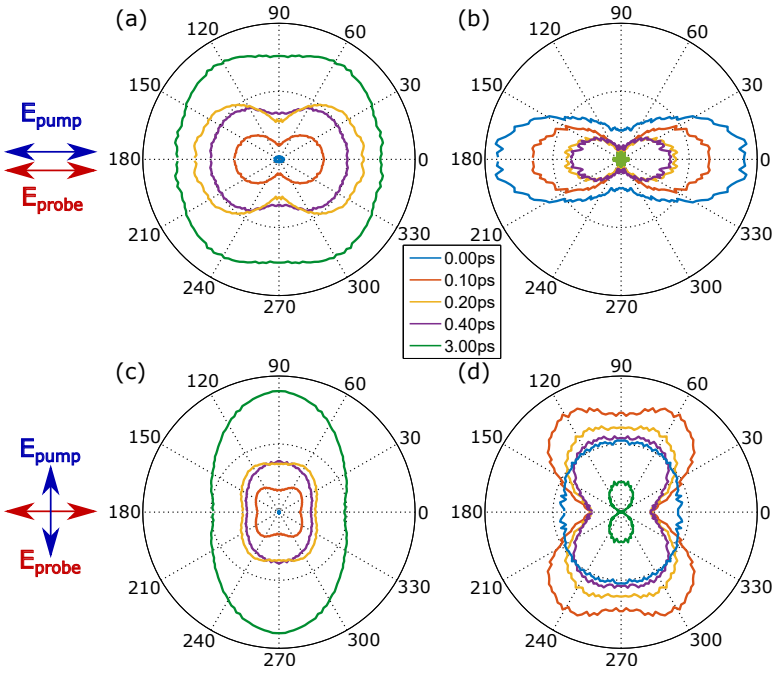

Figure 3.10: NO^+ angular distribution in lab frame with low kinetic energy 0.0 – 0.06 eV, (a) and (c), and high kinetic energy (0.6 – 1.8 eV), (b) and (d). Radius axis shows the ion yield at corresponding angle. The left inserts show the laser polarizations relative to the axis.

four-lobe structure for the perpendicular polarizations. As the delay increases, these features become less distinct. At 3.0 ps, these two-lobe or four-lobe structures are no longer observable. The 400 nm pump pulse selectively excites molecules whose O-O axis is aligned with the laser polarization [8]. Ionization of this aligned ensemble of excited molecules causes the emission patterns of NO^+ at short pump-probe delay. Disappearance of these features indicates that the initial alignment of the NO_2 molecule is lost over time. We estimate that the rotational wavepacket of NO_2 at a temperature of 50 K becomes out of phase in about 1 ps. In our experiments, the NO_2 temperature is 105 K, which means the dephasing time is shorter. Both the excited but bound molecules and the slowly dissociating molecules can rotate as the delay increases and contribute to the disappearance of the patterns.

In Fig. 3.10(b) and (d) we show the angular distribution for the high energy channel for parallel and perpendicular pump probe polarizations respectively. For parallel pump and probe polarizations, shown in Fig. 3.10(b), the angular distributions remain qualitatively unchanged at least 400 fs after excitation. The NO^+ are emitted along the polarization. To identify whether the alignment of the NO-O axis is caused by the exci-

tation or the ionization pulse, we turn to the perpendicular polarizations. Figure 3.10(d) shows that the alignment at 3.0 ps is clearly along the pump polarization, which indicate that the alignment induced by excitation remains for at least 3.0 ps. Two situations can lead to such long-lived alignment: (i), the molecules undergo prompt dissociation; and (ii), the molecule is populated to a metastable excited state with a large internuclear separation. For both cases, the molecules become large within short time and therefore remain aligned for long pump-probe delay.

Prompt dissociations can be induced by multiphoton absorption of the 400 nm pump. Two-photon absorption excites NO_2 to the $(2)^2B_2$ state. Dissociation from the $(2)^2B_2$ state into $NO(^2\Pi_\Omega) + O(^1P_J)$ can result in 1.5 eV total kinetic energy of the neutral fragments [32]. However, in a prompt dissociation, most molecules fragment shortly after the excitation pulse. Thus, the number of NO molecules in the interaction region is expected to remain constant after a few hundred femtoseconds. Therefore, the NO^+ yield should also be constant at long delays. In contrast, we observe a steady decrease of NO^+. To produce a decreasing yield of NO^+ at long delays, the dissociation product NO needs to be in an unstable excited state that decays within a few picoseconds.

On the other hand, if the NO_2 molecules are excited to a metastable state by absorbing one or multiple 400 nm photons, the population in this metastable state could transfer to other states within picoseconds, causing a decreasing ion yield in this channel. Single photon absorption excites NO_2 to the $\tilde{A}^2B_2$ state. The delay-dependent ion yield is in good agreement with the population in the $\tilde{A}^2B_2$ state calculated by Arasaki *et al.* [33]. However, equilibrium geometry of the $\tilde{A}^2B_2$ state is not large enough to keep the molecules aligned for 3 picoseconds. NO_2 can also be excited to the $(4)^2A$ state through two-photon absorption. The $(4)^2A$ state is weakly bound at large bond length [32, 42] and might contribute to this channel.

3.5 Probing with double ionization

Dissociative potential energy surfaces of a singly charged ion can be shallow and produce fragments with low kinetic energy even at small bond lengths. Using such a channel to identify stretched neutral molecules, which often produces low energy fragments from any potential energy surfaces due to large internuclear separation, can be difficult. Removing additional electrons usually transfers the molecules to a steeper potential energy surface, where the molecular bond lengths are better mapped on to the kinetic energy of the fragments. In the following results, the probe pulses doubly ionize the excited NO_2 molecules allowing geometric information to be directly extracted.

Figure 3.11(a) shows the total ion kinetic energy release of channel $NO_2 \rightarrow (NO_2)^* \rightarrow NO^+ + O^+ + 2e$. We observe a clear line with decreasing energy, marked with a dashed

arrow in the figure. Additionally, we observe a weak dissociation channel, marked with a solid arrow. The kinetic energy in this weak channel decreases faster with pump-probe delay than the dominant channel (dashed arrow), and thus comes from a quicker dissociation process. Most importantly, we observe a broad distribution in the kinetic energy distribution (area above dashed arrow in Fig. 3.11(a)). Such a broad distribution shows that the NO-O distance is long, but the elongation does not lead to prompt dissociation. This agrees with our expectation of a slow statistical dissociation process.

We simulate dissociation of neutral NO_2 on the ground electronic state using classical methods. (See details of simulation in Section 3.2.) Assuming that the interaction between NO^+ and O^+ is purely Coulombic, we obtain the kinetic energy release using $1/R_{NO-O}$, shown in Fig. 3.11(b). Although the NO^+-O^+ interaction is not Coulombic at short bond length, this approximation becomes appropriate as the NO-O distance increases. Comparing Fig. 3.11(a) and (b), we observe that kinetic energy release of most events in the experiments is within the same range as in the simulation. Since the excitation energy determines how fast the molecules can dissociate, we can conclude that all the events in Fig. 3.11(a) above the dashed arrow are from a single 400 nm photon pump, whereas the prompt channel, marked with the solid arrow, requires two or more 400 nm pump photons. Experimentally, we observe a strong signal near the outer boundary of single photon dissociation (dashed arrow). This suggests preferential ionization by the probe pulse.

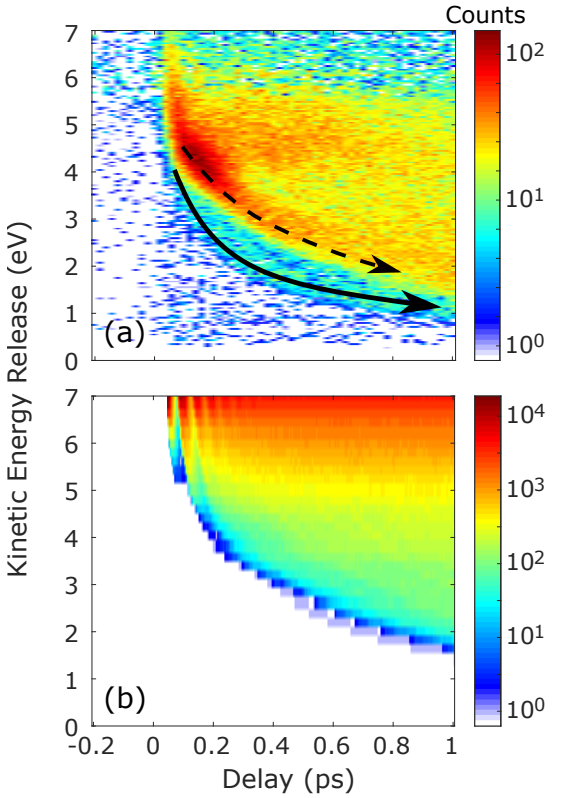

Figure 3.11: (a) Experimental and (b) simulated kinetic energy release of NO^+ and O^+. Dashed and solid arrow shows single and multiphoton dissociation. The simulation assumes single photon excitation by the 400 nm pump.

Some of the single photon excited molecules dissociate quickly. They are marked with a dashed arrow. Others will spend more time exploring different rovibrational levels. We distinguish these molecules by their kinetic energy release and plot their angular distribution at different delays.

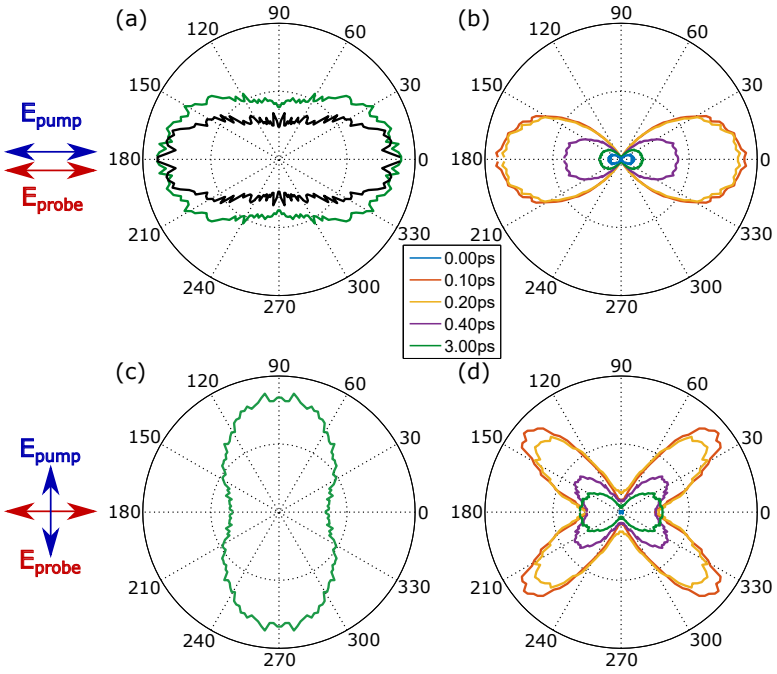

Figure 3.12: Angular distribution of NO^+-O^+ with low kinetic energy (<2 eV) (a) and (c), and high kinetic energy release (3.5eV – 5.5 eV) (b) and (d). Corresponding pump and probe polarizations are shown on the left. Black curve is simulated angular distribution of NO and O dissociation direction, with initial O-O axis along 0-180 degrees. The left inserts show the laser polarizations relative to the axis.

Figure 3.12(a) and (c) are for the relatively fast dissociating molecules (KER < 2 eV) at 3.0 ps using parallel and perpendicular pump-probe polarizations. Figure 3.12(b) and (d) show the distributions for the slow statistical dissociation (3.5 eV < KER < 5.5 eV, or 5.0 a.u. < R_{NO-O} < 7.8 a.u.) for parallel and perpendicular polarizations respectively.

For the low energy fragments, at 3.00 ps, most NO^+-O^+ are aligned with the pump polarization. This angular distribution agrees well with our simulated results, see black curve in Fig. 3.12(a). In the simulation we place the initial O-O axis of each molecule parallel to the pump polarization. The results show that even with perfect initial alignment, the angular distribution for the dissociation is broadened due to rovibrational energy redistribution. Experimentally, the angular distribution is wider in the direction perpendicular to pump polarization. This is because the alignment of the NO_2 molecules by the pump pulse has a broader distribution than in the simulation.

Next, we discuss the slowly dissociating molecules. At short pump-probe delay, most molecules have their O-O axis aligned with the pump pulse because of excitation

selection. Ionization with laser polarization along or perpendicular to the O-O axis results in completely different patterns. Similar to the single ionization results, the double ionization angular distributions also show two and four-lobe symmetry for parallel and perpendicular polarizations, and the features are even sharper than in the single ionization case. This might be because ionization of the second electron introduced additional bias. As delay increases, the difference between the two polarization situations decreases. Both cases end up with very similar two-lobe distributions, which indicates the disappearance of alignment. Two effects contribute to the disappearance of alignment: the rovibrational redistribution and the overall rotation of the molecules. These two effects are coupled and cannot be separate in our results.

3.6 Probing with Coulomb explosion

A two-body breakup provides information on the NO-O distance. To obtain the geometry of the triatomic molecule in 3D, we need to ionize the NO_2 to a high charge state to induce a three-body breakup. In this section, we probe the photodissociation of NO_2 by removing 4 electrons from the molecule and measuring the resulting fragment ions.

The pump pulse used in this section remains the same as in previous sections, but the probe pulse has a higher intensity of 1.8×10^{15} W/cm^2 to remove more electrons from the molecule. The polarizations of the two beams are parallel, both along the time-of-flight axis. The pump-probe delay is scanned from -100 fs to 300 fs with steps of 10 fs. Within this range of delays, we expect that most of the dynamics take place around the conical intersection, and that the NO-O distance does not increase significantly.

3.6.1 Two-body breakups

Since we are using a stronger probe pulse than in the previous section, we first check two two-body breakup channels, $NO_2^{2+} \rightarrow NO^+ + O^+$ and $NO_2^{4+} \rightarrow NO^{2+} + O^{2+}$, to compare to the previous results. Figure 3.13 plots their kinetic energy release. Results from the two channels are very similar, and agree with the results shown in the last section. The weak, prompt dissociation is clearer in the 4+ charge channel.

3.6.2 Three-body breakup

Next, we focus on a three-body breakup channel, $NO_2^{4+} \rightarrow O^+ + N^{2+} + O^+$. Since the two O^+ fragments are identical, both their time-of-flight and positions overlap. We call the O^+ arriving first on the detector the 1st O^+, and the one arriving next the 2nd O^+.

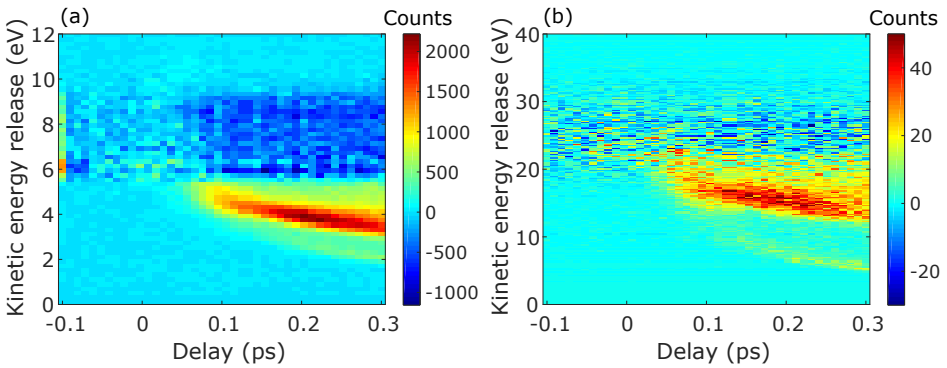

Figure 3.13: Kinetic energy release of (a) $NO_2^{2+} \rightarrow NO^+ + O^+$ and (b) $NO_2^{4+} \rightarrow NO^{2+} + O^{2+}$. The two channels show similar decreasing kinetic energy release. The negative signal indicates a decrease of ground state population.

A maximum sum momentum of 16 a.u. for the three ions is used to select fragments from the same molecules.

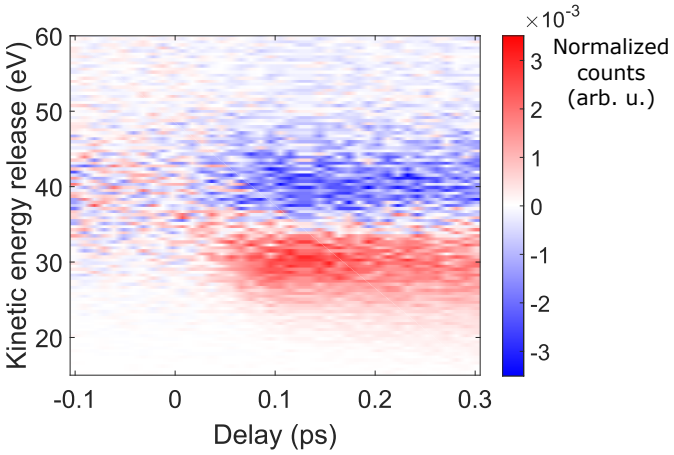

Figure 3.14: Kinetic energy release of $NO_2^{4+} \rightarrow O^+ + N^{2+} + O^+$ as a function of pump-probe delay. Signal is normalized to the total number of events in the channel at each delay.

Figure 3.14 shows the kinetic energy release of the channel $NO_2^{4+} \rightarrow NO^{2+} + O^{2+}$. The signal is normalized to the total number of events in each delay. The positive values (red) indicate that the signal is from molecules that are excited by the 400 nm pump pulse, and the negative values (blue) mean depletion, that is, decreased amount of ionization from the unexcited molecules. Similar to the two-body breakup channels,

we observe a decreasing kinetic energy release in this three-body breakup channel, but the decrease from 0.1 ps to 0.3 ps does not seem as obvious. Another difference between this channel and previous channels is that the signal does not peak at 0.2 ps.

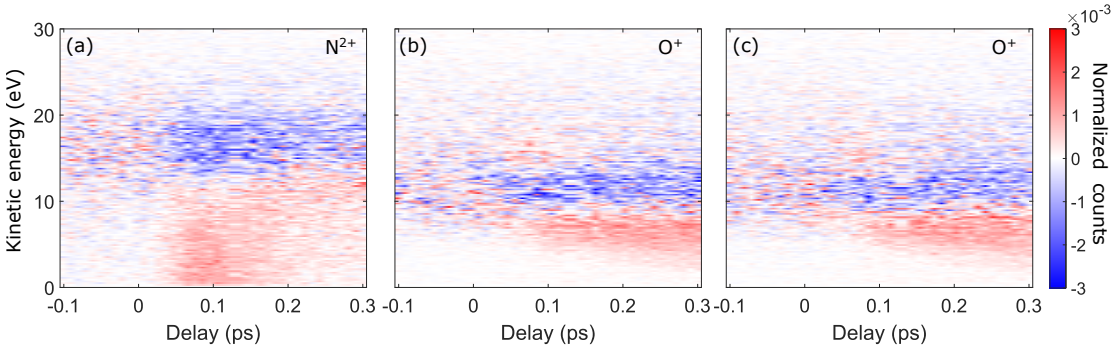

Figure 3.15: Kinetic energy of each fragment in the channel $NO_2^{4+} \rightarrow O^+ + N^{2+} + O^+$.

In Fig. 3.15, we plot the kinetic energy of each fragment in the channel $NO_2^{4+} \rightarrow O^+ + N^{2+} + O^+$. At about 0.1 ps, the N^{2+} fragments have very low kinetic energy, and become more energetic from 0.1 to 0.3 ps. To obtain a low kinetic energy in a Coulomb explosion, a fragment can either be far away from the other fragments, where the Coulomb forces from other fragments are weak, or be in the center of the molecule, where the forces from other fragments cancel each other. At 0.1 ps, the nitrogen atom is unlikely to be far away from the other two oxygen atoms. Therefore, the geometry of the NO_2 must be close to linear so that the forces from the O^+ can cancel. At longer delays, 0.2 - 0.3 ps, the kinetic energy of the O^+ fragments decreases, which indicates a stretch of the N-O bond. However, if the N-O bonds stretch linearly and symmetrically, the energy of N^{2+} will remain low, which is contrary to our observation. Therefore, the NO_2 stretches asymmetrically, and probably bends as the bond stretches.

Figure 3.15 shows the behavior of the three fragments individually, but no correlation between them, which makes it difficult for us to infer the overall picture. For example, both O^+ ions have decreasing energy from 0.1 to 0.3 ps, but this does not mean that the energy of both O^+ in a molecule decrease simultaneously. To study the molecular geometry, we plot the three fragments in correlation on a Dalitz plot [43, 44, 45].

On a Dalitz plot, we use the fraction of energy, $\epsilon = KE_i/KER$, where KE_i is the kinetic energy of the ith fragment. The y axis of a Dalitz plot shows the fraction of energy of one fragment, $\epsilon_1 - 1/3$, and the x axis shows the difference between the energy fraction of the other two fragments, $(\epsilon_2 - \epsilon_3)/\sqrt{3}$. If the three fragments are identical, the dissociation events will be in a circle with a radius of 1/3 [44]. For the channel $NO_2^{4+} \rightarrow$

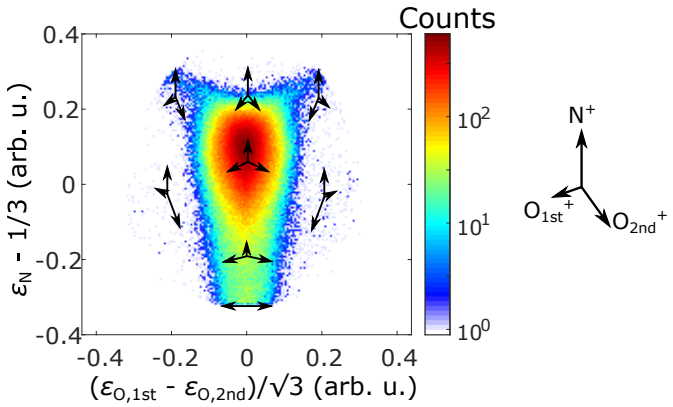

Figure 3.16: Dalitz plot for channel $NO_2^{4+} \rightarrow O^+ + N^{2+} + O^+$ without the pump pulse. The momentum vectors for various points on the Dalitz plot are illustrated. Ion species of the momentum vectors are shown in the right side insert.

$O^+ + N^{2+} + O^+$, we plot $\epsilon_{N^{2+}} - 1/3$ on the y axis, and $(\epsilon_{O,1st} - \epsilon_{O,2nd})/\sqrt{3}$ on the x axis.

Figure 3.16 shows a Dalitz plot for the NO_2 without excitation. Each point on a Dalitz plot corresponds to a set of momentum vectors, with a few examples shown in Fig. 3.16. Along the vertical line in the center, $\epsilon_{O,1st} - \epsilon_{O,2nd} = 0$, the two O^+ ions have equal kinetic energy, indicating a symmetric geometry. As an event goes further to the side, the geometry is more asymmetric.

Figure 3.17 shows Dalitz plots for a few individual delays. The background is removed by subtracting averaged results from negative delays. For each delay, the signal is normalized to the total number of events in the same channel at that delay. At 0.1, 0.2, and 0.3 ps, we observe a decrease (blue) near the center of the Dalitz plot, which corresponds to the ground state equilibrium geometry of NO_2, whereas the increased signal (red) moves from the bottom middle to the top corner. The bottom middle of the Dalitz plot corresponds a symmetric linear geometry. The top corner means one O^+ has low energy, and therefore is either far away or between the other two fragments. Considering that the molecule is linear with the nitrogen atom in the middle at 0.1 ps, the low energy O^+ is more likely to be away from the other fragments. This confirms the asymmetric geometry of NO_2 with a large O-NO distance.

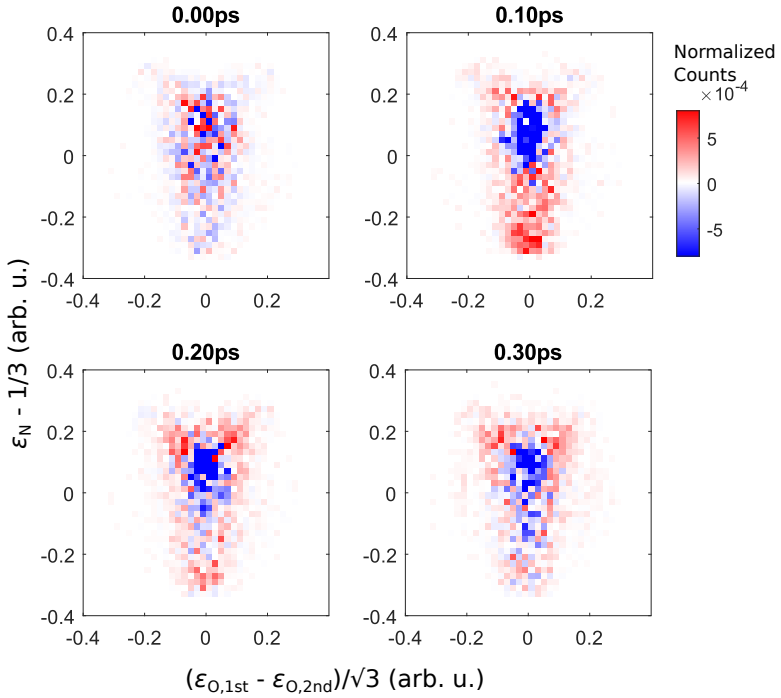

Figure 3.17: Normalized Dalitz plots for the channel $NO_2^{4+} \rightarrow O^+ + N^{2+} + O^+$ at several pump-probe delays. For each delay, we first subtract the background data, that is, the averaged data at negative delays, and then normalize to the total number of events in the channel at that delay.

3.7 Summary

We studied the photodissociation dynamics of NO_2 initiated by a 400 nm pulse through multiple probe channels. We followed the evolution of the intermediate states to their final products via the time-dependent kinetic energy release, the photo-ion angular distributions, the evolution of the ion yield, and the Dalitz plots.

In our view, the most intriguing aspect of these experiments is the observation that, in the double ionization channel, the $NO^+ + O^+$ Coulombic recoil kinetic energy decreases with time delay. This must be related to the average increase of NO-O distance as the excited system explores the ground state phase space on its way to separated products. The Coulomb explosion kinetic energy release varies inversely with distance between fragments. We suggest that this measure is a unique probe of the average NO-O distance during the statistical unimolecular decay of NO_2. In fact, we are not aware of any other observable which directly probes the evolution of the average distance between fragments

during a statistical decay. By combining these COLTRIMS results with high accuracy ground state classical trajectory studies, one could confirm this intriguing suggestion.

Coulomb explosion imaging is a unique way to probe nuclear dynamics with high spatial and temporal resolutions. However, the collection rate in these experiments is generally lower than the laser repetition rate to guarantee that at most one molecule is exploded in each laser shot. As a result, the experimental observations are often limited by a lack of events. In this chapter, we showed results with up to 4 electrons removed from NO_2. Channels with higher charge states were also observed, but the signal-to-noise ratio for those channels was poor. In the NO_2 statistical photodissociation, the geometries of the excited molecules vary from one to another, and thus require even higher statistics. Therefore, laser systems with higher repetition rates, for example 100 kHz, are needed to further explore transient state nuclear dynamics.

Chapter 4

Dissociation of CO^{2+} in a Dimer

4.1 Clusters

Clusters are intermediate between single molecules and solids. A cluster consists of multiple neutral molecules. A dimer is the simplest form of a cluster and consists of two component molecules. In many dimers, the component molecules are held together by van der Waals forces. The van der Waals forces are weak and they arise from the temporal fluctuation of electronic charges inducing transient dipoles. Van der Waals interactions are ubiquitous in nature and important for many physical and chemical phenomena [46].

Though very weak, van-der-Waals and electrostatic interactions can have a critical influence on the decay of electronic excitation in a cluster. A prominent example is the interatomic Coulombic decay (ICD) [20], where electronic excitation is efficiently transferred over a large distance within a dimer [47, 48, 19] to allow for a fast non-radiative relaxation.

In this chapter, we show that in a van der Waals complex, a different rapid decay mechanism exists, which does not involve the transfer of electronic excitation. Specifically, we observe a prompt dissociation of metastable CO^{2+} in the triply charged dimer $(CO)_2^{3+}$ and show it is a direct consequence of the weak interactions in the complex [49].

4.1.1 $(CO)_2$

Clusters exist at low temperatures. In our experiment, the carbon monoxide clusters are generated in the supersonic expansion of pure CO gas at 5 bar backing pressure through a 10 μm diameter nozzle. The nozzle is cooled to 120 K. Based on our ion mass spectra, we estimate that about 5% of all events originate from $(CO)_2$.

Spectroscopy studies have shown that the $(CO)_2$ features a planar anti-parallel geometry with either carbon atoms or oxygen atoms in the middle [50, 51], see Fig. 4.1. The intermolecular separation is about 4.4 Å for the C-bonded isomer, and 4.0 Å for the O-bonded isomer. The energy difference between the isomers is very small. In the ground vibrational state, the C-bonded isomer is only lower in energy by 0.88 cm^{-1} than the O-bonded isomer [50]. With energy of the order of cm^{-1}, the dimers can easily change from C-bonded antiparallel form to T-shaped, or O-bonded form [51]. We estimate the $(CO)_2$ temperature in the supersonic jet to be 9 K. $(CO)_2$ has 6 vibrational degrees of freedom, corresponding to energy of $3k_BT$, that is, 19 cm^{-1}. Therefore, we expect the dimers to have different forms.

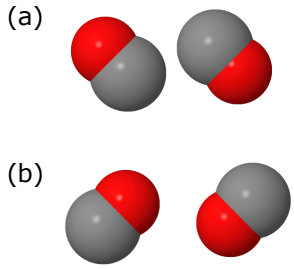

Figure 4.1: Geometry of (a) C-bonded and (b) O-bonded CO dimer. Carbon atoms are in grey and oxygen atoms in red. Both isomers are planar.

4.2 Monomer CO^{2+} dissociation

Before discussing the dimer dissociation, let us first consider the monomers. The monomer CO^{2+} has been extensively investigated as a model system of a metastable molecular dication (e.g., [52, 53, 54, 55] and refs. therein). The lowest electronic states, the $X^3\Pi$, $a^1\Sigma^+$, and $b^1\Pi$ states, are metastable. The lifetimes of these states range between tens of picoseconds to seconds [52, 53, 54, 55, 56, 57].

The highest occupied molecular orbital (HOMO) and HOMO-1 of CO are the (fully occupied) 1π and 5σ, respectively. The ground electronic state of CO^{2+}, the $X^3\Pi$ state, arises from a $1\pi^3 5\sigma^1$ electronic configuration where one electron from HOMO and one from HOMO-1 are removed. The dissociative $^3\Sigma^-$ state arises from a $1\pi^2 5\sigma^2$ electronic configuration, where two electrons from HOMO-1 are removed. CO^{2+} in the $X^3\Pi$ state can dissociate through spin-orbital coupling with the $^3\Sigma^-$ state, producing fragments with total kinetic energy of about 6 eV.

Experimentally, we have monomers and dimers in the same jet. This allows us to measure the dissociation of monomers and dimers under the same conditions. Figure 4.2 shows the kinetic energy release of $CO^{2+} \rightarrow C^+ + O^+$. The peak at 6.2 eV is mostly from the $X^3\Pi$ state. Dissociation from the $a^1\Sigma^+$, and $b^1\Pi$ state also contribute to this peak. The peak at about 8 eV corresponds to dissociation from $A^3\Sigma^+$ state [53, 58, 59].

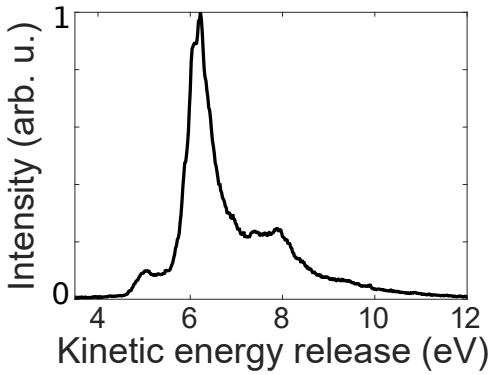

Figure 4.2: Total kinetic energy release of $CO^{2+} \rightarrow C^+ + O^+$

4.3 Dimer breakup channels

We use a circularly polarized 800 nm, 25 fs pulse to ionize the molecules. The peak intensity of the pulse is 6×10^{14} W/cm^2. The laser pulse removes multiple electrons from the dimer and we detect the fragments in COLTRIMS (see section 2.1 for more details). We observe different breakup channels.

4.3.1 $(CO)_2^{2+} \rightarrow CO^+ + CO^+$

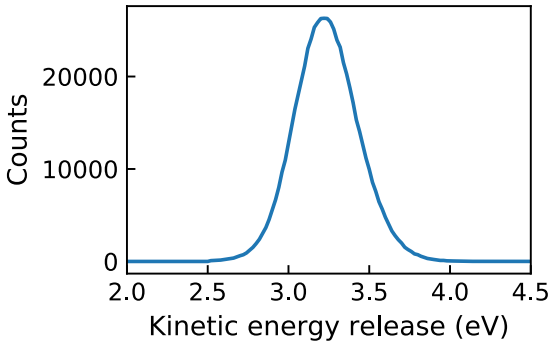

Figure 4.3: Total kinetic energy release of $(CO)_2^{2+} \rightarrow CO^+ + CO^+$

First, we study a two-body breakup channel of the dimer, $(CO)_2^{2+} \rightarrow CO^+ + CO^+$. To select events from this channel we restrict the sum momentum of the two fragments to be smaller than 10 atomic units (a.u.) and the momentum of each fragment is larger than 40 a.u.. Figure 4.3 shows the total kinetic energy release of the two CO^+ fragments. The

kinetic energy originates from potential energy of the fragments right after ionization. Since the intermolecular separation is large (4.0 $\sim$ 4.4 Å), we assume that the two CO^+ ions repel each other only through the Coulomb potential. Therefore, the distance between the two component CO molecules can be calculated as:

$$R = \frac{q_1 q_2}{KER} \tag{4.1}$$

where q_1 and q_2 are the charge of the two ions, and all parameters are in atomic units. From the kinetic energy release of 3.2 eV, we obtain a bond length of 4.5 Å, which agrees well with our expectation.

4.3.2 $(CO)_2^{3+} \rightarrow C^+ + O^+ + CO^+$

For the three-particle breakup channel, $(CO)_2^{3+} \rightarrow C^+ + O^+ + CO^+$, we select events where the sum momentum of the fragments is low ($|\mathbf{p}_{C^+} + \mathbf{p}_{O^+} + \mathbf{p}_{CO^+}| < 10$ a.u.) and their relative momentum is high ($|\mathbf{p}_{C^+} - \mathbf{p}_{O^+}| > 50$ a.u. and $|\mathbf{p}_{CO^+}| > 40$ a.u.) to make sure the fragments are correlated, i.e., from the same dimer.

The distribution of CO^+ momentum is shown in Fig. 4.4(a). The CO^+ momentum has a narrow peak between 100 a.u. and 120 a.u. on top of a wide distribution from 40 to 170 a.u.. We fit the momentum distribution to the sum of two Gaussian functions, shown as blue and red curves in Fig 4.4(a).

In our measurements, each ion is treated as a point charge. The three point charges repel each other within the plane defined by the three points. As a result, their momenta also remain in this plane. Therefore, for the three-particle breakup, we can plot the 3-dimensional momentum of the fragments in a 2-D histogram. In Fig 4.4, we define the direction along the momentum of CO^+, $\mathbf{p}_{CO^+}$, as $p_\parallel$, and the momentum of O^+, $\mathbf{p}_{O^+}$, as the positive direction of the $p_\perp$ axis. Such a 2-D histogram is called a Newton diagram. Each pixel on this diagram corresponds to the end of a momentum vector, and the colour scale shows the number of events in that pixel.

The Newton diagram in Fig. 4.4(b) shows a ring and a cone structure. Since we also observe two peaks in the CO^+ momentum distribution, we separate the data into two subsets based on $|\mathbf{p}_{CO^+}|$, and plot the Newton diagram for each subset in Fig 4.4(c) and (d). Subset I corresponds to the broad peak, $|\mathbf{p}_{CO^+}| < 100$ a.u. or $|\mathbf{p}_{CO^+}| > 120$ a.u., and subset II is mostly the narrow peak, 100 a.u. $< |\mathbf{p}_{CO^+}| < 120$ a.u.. We observe that the structures in the Newton diagram are also separated in the two subsets. Some cone structure shows up in subset II due to the imperfect separation. Table 4.1 shows the number of events and the contamination ratio for each subset in its respective momentum range. The narrow peak, subset II, has very few events in $|\mathbf{p}_{CO^+}| < 100$ a.u. or $|\mathbf{p}_{CO^+}| >$ 120 a.u.. In contrast, the broad peak, subset I, accounts for a significant background in

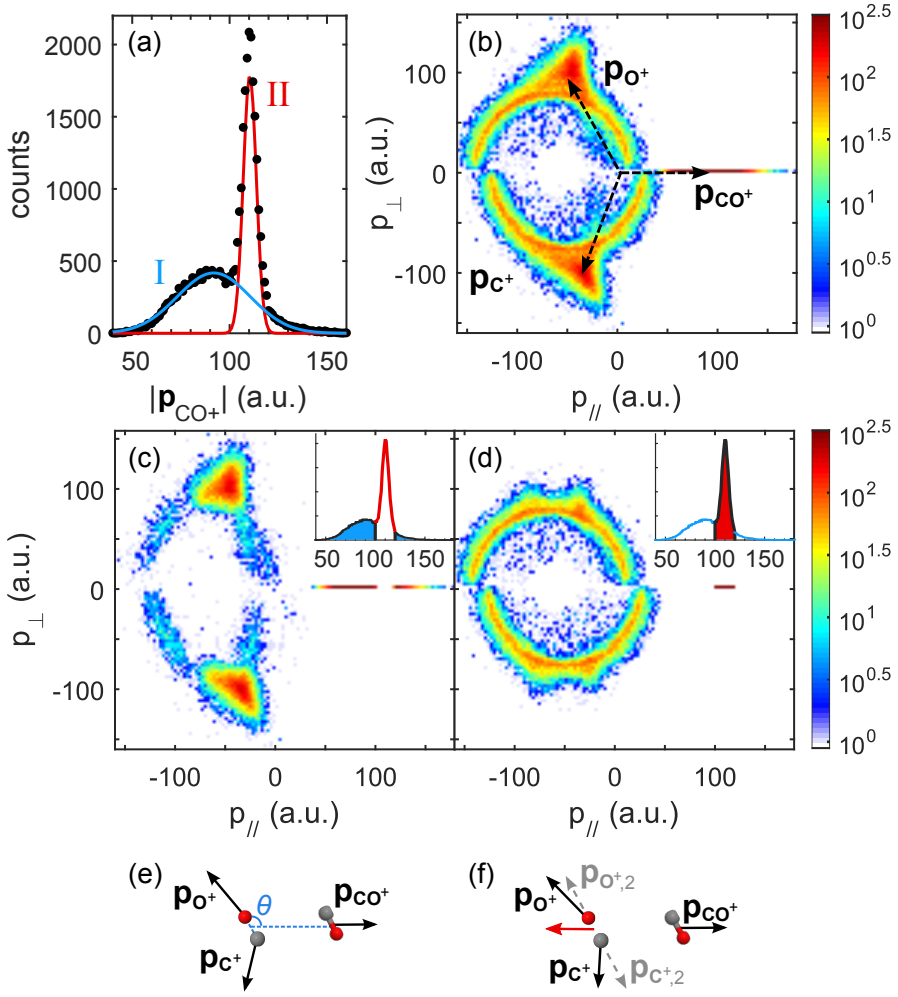

Figure 4.4: (a) Momentum distribution of CO^+. Black dots show experimental data; red and blue curves show the fitting with two Gaussian distributions. (b) Newton diagram for all events in the channel $(CO)_2^{3+} \rightarrow C^+ + O^+ + CO^+$. (c)-(d) are Newton diagrams for events in different subsets. Corresponding CO^+ momentum is shown in the top right insert figures. (c), $|\mathbf{p}_{CO^+}|$ <100 a.u. or $|\mathbf{p}_{CO^+}|$ > 120 a.u.; (d), 100 a.u. < $|\mathbf{p}_{CO^+}|$ < 120 a.u.. (e) and (f) are sketches of direct and sequential dissociation processes. Black arrows, the final momentum of each fragment; red arrow, momentum of CO^{2+} in the first dissociation step; grey arrows, momentum of C^+ or O^+ from the second dissociation step. Geometry with minimum energy is shown as an example.

$\lvert\mathbf{p}_{CO^+}\rvert$ (a.u.)	Events in subset I	Events in subset II	Contamination ratio
100–120	5×10^3	1.5×10^4	25%
30–100, 120–200	1.4×10^4	36	0.26%

Table 4.1: Number of events in subsets of $(CO)_2^{3+} \rightarrow C^+ + O^+ + CO^+$.

the CO^+ momentum in the range of 100 – 120 a.u., which also shows up in the Newton diagram in Fig. 4.4(d).

The structures in the Newton diagram in Fig. 4.4 indicate that the fragments interact in different ways during the breakup. The ring structure suggests a sequential breakup, where the dimer first breaks into CO^+ and CO^{2+}, and the CO^{2+} dissociates into C^+ and O^+ afterwards. If the delay between the two dissociation steps is long, the CO^+ will have little effect on the dissociation of CO^{2+}. In that case, the second dissociation step provides the same momentum for the C^+ (or O^+) regardless of the orientation of CO^{2+} relative to the van der Waals bond. Thus, a ring is formed in the momentum diagram. The cone structure, on the other hand, requires interaction of all three fragments at the same time.

In the sequential breakup, the half-rings for the momentum of C^+ and O^+ are shifted. This is due to the mass difference between the two fragments. Before the CO^{2+} dissociates, the C and O have the same velocity, and therefore different momenta, which results in the shift in their momentum distribution.

Sequential and nonsequential dissociations have been previously observed in ArCO [60]. However, the mechanism behind them has not been discussed.

Sequential breakup

To confirm subset II is a sequential process, we compare it to a two-particle breakup: a CO dimer breakup into two singly charged monomers, $(CO)_2^{2+} \rightarrow CO^+ + CO^+$.

The first step of the sequential breakup is $(CO)_2^{3+} \rightarrow CO^+ + CO^{2+}$. Since one ion is doubly charged, the CO^+ has twice the kinetic energy of the fragment in channel $(CO)_2^{2+} \rightarrow CO^+ + CO^+$. To compensate for the difference, we multiply the kinetic energy of CO^+ in the latter channel by 2 and compare the two channels in Fig. 4.5(a). Furthermore, we subtracted the background in subset II, assuming a linear contamination from subset I. Figure 4.5 shows the kinetic energy distributions for the two channels overlap very well. This confirms that subset II is a sequential process, where CO^{2+} does not dissociate until the CO^+ attains the asymptotic momentum from the two-body Coulomb interaction.

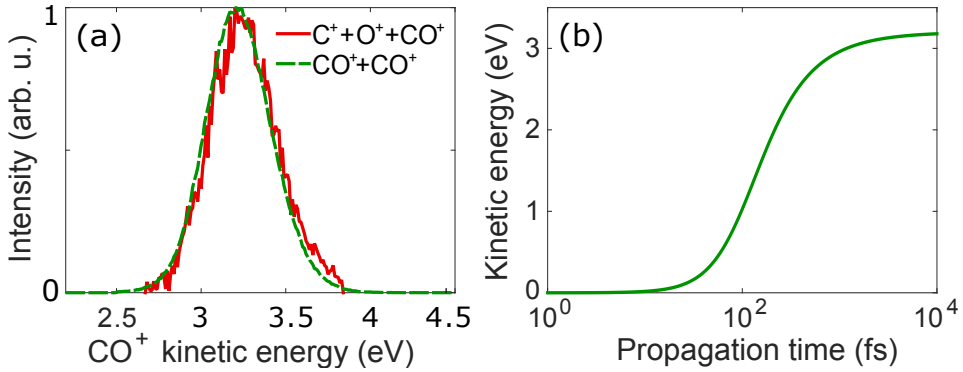

Figure 4.5: (a) Kinetic energy distribution of CO^+, solid red curve for the sequential dimer breakup $(CO)_2^{3+} \rightarrow C^+ + O^+ + CO^+$ (subset II) and dashed green curve for the two-particle dimer breakup $(CO)_2^{2+} \rightarrow CO^+ + CO^+$. Kinetic energy for the latter channel is multiplied by 2 to compensate for the charge difference in the two channels. (b) Kinetic energy of CO^+ in the breakup channel $(CO)_2^{3+} \rightarrow CO^{2+} + CO^+$ as a function of propagation time.

To estimate the time delay between the two steps in the sequential breakup, we simulate the breakup process $(CO)_2^{3+} \rightarrow CO^{2+} + CO^+$. We assume both fragments are point charges with mass, and their motions are only affected by Coulomb field of the other ion. The fragments start with zero momentum, and we propagate them by solving the kinematic equations:

$$\begin{cases} \dfrac{d\vec{x}_1}{dt} = \dfrac{\vec{p}_1}{m_1} \\ \dfrac{d\vec{x}_2}{dt} = \dfrac{\vec{p}_2}{m_2} \\ \dfrac{d\vec{p}_1}{dt} = \dfrac{q_1 q_2}{|\vec{x}_1 - \vec{x}_2|^2} \cdot \dfrac{\vec{x}_1 - \vec{x}_2}{|\vec{x}_1 - \vec{x}_2|} \\ \dfrac{d\vec{p}_2}{dt} = \dfrac{q_1 q_2}{|\vec{x}_2 - \vec{x}_1|^2} \cdot \dfrac{\vec{x}_2 - \vec{x}_1}{|\vec{x}_2 - \vec{x}_1|} \end{cases} \tag{4.2}$$

where $\vec{x}$ and $\vec{p}$ are the position and momentum, with the subscripts denoting fragments. $q_1 = 2$ and $q_2 = 1$ are the charge, and $m_1 = m_2$ are mass of CO. Since we only have 2 fragments, the simulation is done in 1D.

Figure 4.5(b) shows the kinetic energy of CO^+ as a function of propagation time. The simulation shows that it takes about 1 ps to convert the Coulomb potential energy to kinetic energy of the fragments. Therefore, we conclude that the CO^{2+} in the sequential dimer breakup channel has a lifetime longer than 1 ps, and that CO^{2+} in the direct channel dissociates within 1 ps.

Fitting geometry of dimers in direct channel

We fit the geometry of each dimer in the direct channels with an iterative algorithm [14, 13]. We use three parameters to describe the geometry of a dimer: length of the van der Waals bond, R, CO molecular bond length, r_{CO}, and one bond angle θ, as is shown in Fig. 4.4(e). The CO^+ is treated as a point charge.

We start the calculation by guessing structures for the dimer. For each structure, we propagate the fragments forward using a 5th order Runge-Kutta method to obtain their asymptotic momentum. We use an optimization algorithm called a downhill simplex method to minimize the difference between the simulated momentum and the experimental results.

We assume a Coulomb potential between the two CO ions. However, the CO^{2+} potential energy surface is not Coulombic due to the low charge states and short internuclear distance. Therefore, we use the $^3\Sigma^-$ potential from Eland *et al.* [61] between the C^+ and O^+. The potential energy curves are shown in Fig. 4.6.

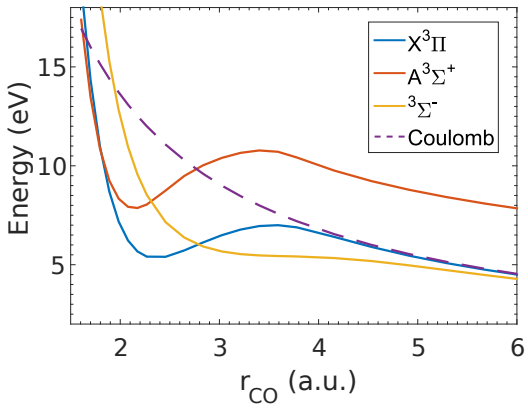

Figure 4.6: Potential energy surface of CO^{2+} from Eland *et al.* [61]. The origin of potential energy is at the asymptotic energy of $^3\Sigma^-$, $E(r_{CO} = \infty) = 0$.

Figure 4.7 shows CO dimer geometry from fitting. In this plot, we keep the center of mass of the CO^{2+} at the origin and the van der Waals bond along x axis. The CO^+ is plotted on the x axis, O^+ on the upper plane and C^+ on the lower plane. Note that each pixel in this figure corresponds to the position of a fragment. The distance between the two CO is about 8.3 a.u., or 4.4 Å, which agrees with previous literature [50] and our results from the two-particle dimer breakup. The CO bond length is 2.3 a.u., or 1.2 Å. The position of C^+ and O^+ also forms a ring. Different from the ring structure in Newton diagram, this shows that in the direct breakup the CO^{2+} orientation can be any angle from 0 to 180 degrees relative to the van der Waals bond, which is along the x axis in Fig. 4.7 (a). Therefore, we confirm that the CO dimers have many different shapes under our experimental conditions.

4.4 CO^{2+} dissociation in dimers vs. in monomers

We observe sequential and direct dissociation of the dimer, corresponding to slow and prompt dissociation of CO^{2+}. As we mentioned in section 4.2, the lifetime of CO^{2+} is on the order of tens of picoseconds for most of the vibrational levels on the lowest electronic states. If the same is true in dimers, we would only observe the sequential channel for the dimer dissociation. Therefore, the prompt CO^{2+} breakup must be a new channel that does not exist in monomers. Next, we will compare the CO^{2+} breakup in the direct channel to the monomer breakup. Since all three fragments interact with each other simultaneously in the direct breakup channel, we cannot obtain the pure kinetic energy release in the C-O bond breaking process. Alternatively, we first compare the sequential channel to the monomer dissociation, and then compare the sequential breakup to the direct breakup channel.

4.4.1 CO^{2+} in sequential dimer breakup

Figure 4.8(a) compares the kinetic energy release of $C^+ + O^+$ from the monomer breakup with the second step of the sequential dimer breakup. In the sequential three-body breakup, the kinetic energy release of the second step is $KE = \frac{1}{2}|\mathbf{p}_{C^+,2}|^2/m_C + \frac{1}{2}|\mathbf{p}_{O^+,2}|^2/m_O$, where $\mathbf{p}_{C^+,2} = \mathbf{p}_{C^+} + \mathbf{p}_{CO^+}(m_C/m_{CO})$ and $\mathbf{p}_{O^+,2} = \mathbf{p}_{O^+} + \mathbf{p}_{CO^+}(m_O/m_{CO})$ are the momenta from the second dissociation step, i.e., the CO^{2+} breakup. The kinetic energy distributions of the two processes are almost identical. Therefore, the CO^{2+} in the sequential dimer breakup channel dissociates along the same electronic states as the monomer CO^{2+}. The kinetic energy for the second step of

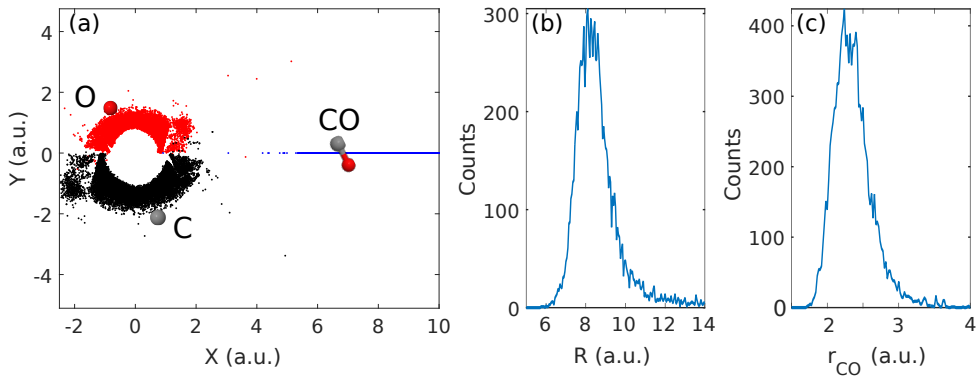

Figure 4.7: (a) Geometry of the dimer on a plane. Each dot represents position of a fragment. (b) Distance between the two CO. (c) Bond length of CO.

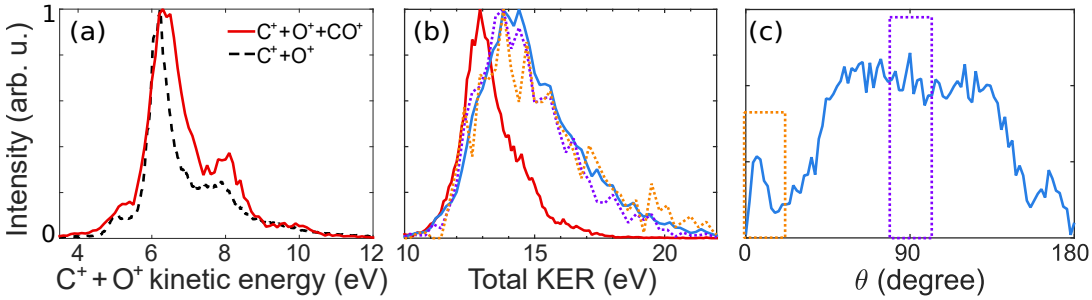

Figure 4.8: (a) Kinetic energy of C^+ and O^+, solid red curve for the second step of dimer sequential breakup, dashed black curve for monomer breakup $CO^{2+} \rightarrow C^+ + O^+$. (b) Total kinetic energy release in the three-particle dimer breakup process. Solid blue curve is for subset I, direct breakup channel; solid red curve for subset II, sequential channel. The dotted curves are for specific geometries in the subset I: orange curve for $\theta <$ 20 degrees and purple curve for $80 < \theta < 100$ degrees. (c) Bond angle distribution of the dimer in the direct dissociation channel, subset I.

the sequential dimer breakup is about 0.2 eV higher than that for the monomer. This is probably because in the dimer, the first breakup step can excite the CO^{2+} vibrationally and rotationally. When CO^{2+} dissociates, the rovibrational energy becomes translational kinetic energy of C^+ and O^+, resulting in slightly higher kinetic energy release.

4.4.2 CO^{2+} in direct dimer breakup

Figure 4.8(b) compares the total kinetic energy release of the fast direct breakup channel (subset I, solid blue curve) to the sequential breakup channel (subset II, solid red curve). The kinetic energy release of the direct channel is about 1.2 eV higher than that of the sequential channel. Figure 4.8(a) shows that the sequential breakup produces fragments in the lowest electronic final states. Hence, the higher kinetic energy release in the direct breakup could be explained by an initial population of higher electronic states in the $(CO)_2^{3+}$ or a dependence on the dimer geometry.

We fit the geometries of the dimers in the direct channels in the previous section. Figure 4.8(c) shows the distribution of the bond angle θ (see Fig. 4.4(e) for the definition of θ). The fitting result shows that θ has a wide distribution between 0 and 180 degrees. Thus, the direct channel does not arise from a specific geometry.

In Fig. 4.8(b) we plot the kinetic energy release of the dimers with bond angle $\theta <$ 20 degrees (dotted orange curve) and $80 < \theta < 100$ degrees (dotted purple curve). The dimers with different bond angles have similar kinetic energy release. This rules out the

possibility that different geometries cause the difference in kinetic energy release of the fast and slow channels.

4.5 Potential energy surface of CO^{2+} in a dimer

To investigate the origin of the dimer-specific fast dissociation channel, we compute potential energy curves for the $(CO)_2^{3+}$ dimer complex using *ab initio* electronic structure methods. We compute these curves using two different approaches. The first assumes that CO^+ is simply a point charge, resulting in perturbed CO^{2+} dissociation curves. The second approach explicitly considers the electronic structure of the CO^+ and computes the potential energy surfaces of the total dimer complex. The calculations were performed employing multireference complete active space (CASSCF) wave functions in conjunction with a multireference configuration interaction (MRCI) treatment of dynamical electron correlation [62, 63].

Figure 4.9(a) illustrates the relevant molecular orbitals and potential energy curves. When the CO^{2+} is in an electric field free environment, molecular symmetry precludes any nonadiabatic coupling between the $X^3\Pi$ and the $^3\Sigma^-$ states. However, a positive charge at a distance of 8 a.u. (the ground state intermolecular distance [51][50]), as illustrated in the top right insert in Fig. 4.9(a), differentially distorts the π_x and π_y orbitals. This breaks the symmetry of the $^3\Pi$ state, and thereby engenders an avoided crossing between one component of the $X^3\Pi$ and the $^3\Sigma^-$ state.

The next two lowest-lying electronic states, $a^1\Sigma^+$ and $b^1\Pi$, are singlet states. For both the monomer and dimer, these states can only couple to the $^3\Sigma^-$ state via spin-orbit interaction. The coupling between these states has been investigated previously in the monomer [56], and is of a magnitude insufficient to account for the short lifetimes required to lead to rapid dissociation. Therefore, we do not consider these states in the following discussion of the direct dissociation channel.

Thus, in contrast to the CO^{2+} monomers, which can only dissociate via spin-orbit coupling, the CO^{2+} in the dimer has a direct adiabatic dissociation channel via the avoided crossing between the $X^3\Pi$ and $^3\Sigma^-$ states. However, the charge-induced avoided crossing does not explain why the kinetic energy release for the fast pathway is higher than that observed for the 'slow' channel.

The assumption that the CO^+ counter ion can be represented as a point charge (thereby neglecting its electronic structure) is tested by computing the dissociation curves of a component CO in the $(CO)_2^{3+}$ complex. As Fig. 4.9(b) illustrates, we observe a new low-lying electronic state for the dimer system, a component of the degenerate ground state of the dimer, not present in the point charge model. This new electronic state

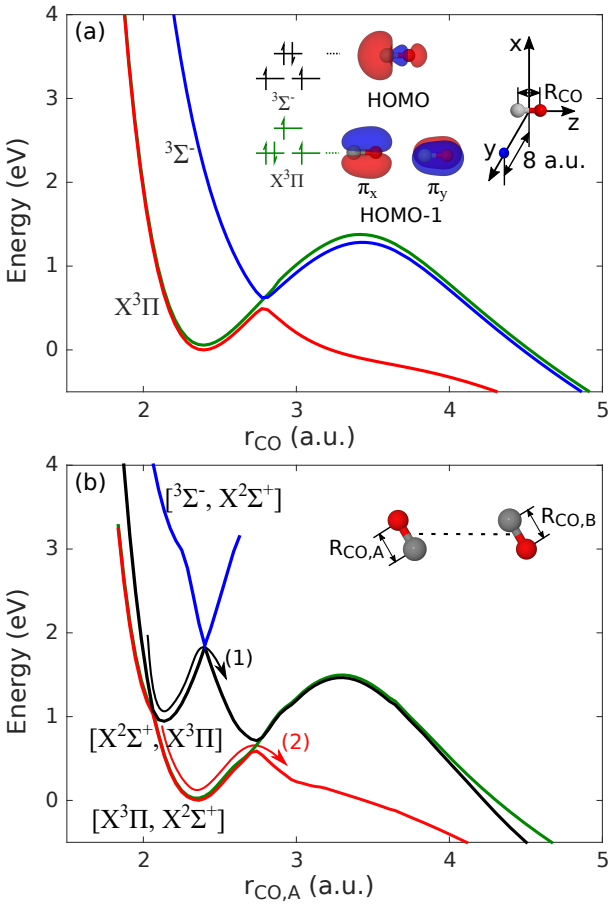

Figure 4.9: (a) Potential energy curves of CO^{2+} with a point charge. The Coulomb field of the point charge perturbs the π_x and π_y orbitals differently, which breaks the symmetry of one $X^3\Pi$ electronic state. An avoided crossing arises between one component of the $X^3\Pi$ states and the $^3\Sigma^-$ state. (b) *Ab initio* potential energy curves of the CO^{2+}-CO^+ complex. Arrows show possible dissociation pathways. Kinetic energy release from pathway (1) is 1.2 eV higher than from pathway (2).

arises from the fact that the different charge states can be located on either one of the constituent CO monomers. Specifically, the dicationic species may localize on either of the two component CO moieties. When the two CO bond lengths are identical, these CO molecules are indistinguishable and the solutions are degenerate, resulting in the curve crossing in Fig. 4.9(b) at $r_{CO,A} \sim 2.1$ a.u. The coupling of states on each component monomer gives rise to a new manifold of electronic states which can be determined from excimer theory [64]. This new excited state of the dimer crosses the dissociative $^3\Sigma^-$

state 1.2 eV above the lower crossing with the ground state. This value is consistent with the observed difference in kinetic energy release of the two channels. Thus, we conclude that the electronic structure of the CO^+ counter ion has a non-negligible influence on the decay dynamics of the triply charged complex.

This picture is fully consistent with previous ArCO results [60]. In particular, computations show that the electronic structure of the Ar atom leads to new dissociation channels in the complex via the coupling of CO^{2+}-Ar^+ and CO^+-Ar^{2+} charge states. The same mechanisms discussed for the $(CO)_2$ dimer can be applied to these previous studies, where the only differences are quantitative and arise from different relative electronic state energies since the ionization potentials of the component CO and Ar are distinct (i.e., in $(CO)_2^{3+}$ they are identical).

4.6 Summary

In our experiments, we observe a new dissociation pathway emerging when CO^{2+} is placed in a van der Waals system with another ion. Compared to the dissociation of CO^{2+} in monomers, which occurs on the time scale of picoseconds or longer, the CO^{2+} in dimers can dissociate promptly and result in higher kinetic energy release. Calculations considering the nearby CO^+ as a point charge suggests that the charge breaks the symmetry of one $X^3\Pi$ state, which then forms an avoided crossing with the dissociative $^3\Sigma^-$ state. Compared to monomers that can only dissociate via the spin-orbit coupling between these states, dissociation via the avoided crossing occurs on a much shorter time scale. Calculations considering the electronic structure of the nearby CO^+ shows that a new low-lying excited dimer state arises from coupling of different charge states on the two component CO molecules. Dissociation from this new state results in high kinetic energy, while the CO^+ fragment will have low internal energy. Future experiments can measure the internal energy of CO^+ for validating our model.

Quick relaxations through interaction with other molecules may apply to other van der Waals systems as well. It has interesting implications in the problem of air lasing. Recently, Britton *et al.* studied N_2^+ lasing using a gas jet in vacuum [65], which avoids the complications of air filamentation. A quick decay in the emission of N_2^+ was observed on a timescale of 200 fs, which is much faster than the usual $\sim$10 ps decay in air that can be attributed to state-mixing by electron-ion collisions. The quicker decay appears to be unique to the jet, where the molecules are cold and can form clusters. Although not characterized in this case, a contribution from the clusters in the emission could be significant due to enhanced ionization [66]. Similar to our experiment, the fast decay may arise from interaction among the molecules in the clusters. Specifically, the energy levels may be shifted randomly by the nearby N_2^+ ions, causing incoherent emission.

Van der Waals interactions are not only key to understanding cluster behavior, but also play an important role in biology such as protein-RNA interactions [67], and in semiconductors such as interactions between nanostructures [68]. Understanding relaxation mechanisms in van der Waals complexes will be a key step in learning about and controlling molecular systems.

Chapter 5

Harmonic generation from solids

5.1 Harmonic generation at high repetition rate

5.1.1 Harmonic generation from gases

High harmonic generation in gases is an important technique for generating extreme ultraviolet attosecond pulses and studying molecular structure and dynamics. It can be described with a semiclassical three-step model:

1. An electron tunnels out of the potential energy barrier lowered by a strong laser pulse.
2. The electron is accelerated by the strong laser field. If the electron is born at the right time in the laser cycle, it will return towards its parent ion.
3. The electron recombines with the ion and emits the kinetic energy that it obtained from the laser field plus the ionization potential of the atom as a high harmonic photon.

The three steps repeat at every half cycle of the driving laser pulse. Due to the change of sign of the driving laser field, the harmonics emitted at successive half-cycles have opposite phase. The phase flip results in destructive interference in harmonics that are even multiples of the driving laser frequency, and constructive interference in odd harmonics. As a result, we only observe generation of odd harmonics from gases when driving with a single-colored multi-cycle pulse.

5.1.2 Frequency comb

A frequency comb is a laser whose spectrum consists of equally spaced lines. It has been used in many precise measurements such as optical atomic clocks and high-precision spectroscopy. Frequency combs are available in infrared and visible, and now harmonic generation provides an opportunity for generating frequency combs in the extreme ultraviolet.

Frequency combs require repetition rates on the order of MHz. Harmonic generation from gases often use Ti:Sapphire systems with repetition rates of kHz. This is because the gas molecules tend to have high ionization potentials; for example, the ionization potential of argon is 15.76 eV. With these gases, one needs a laser intensity on the order of $10^{14}\mathrm{W/cm^2}$ to get a high ionization rate in the first step of harmonic generation, which will otherwise limit the number of harmonic photons. The high intensity requirements limit single-pass harmonic generation to a reduced pulse repetition rate.

One way to increase the repetition rate is to use optical enhancement cavities [69, 70]. Cingoz *et al.* generated high repetition rate frequency combs in the extreme ultraviolet with average power on the order of μW in an enhancement cavity [70]. Their intracavity power of the driving laser is several kW, which requires extremely robust mirrors. Building and maintaining an enhancement cavity is also difficult.

Another way is to reduce the laser intensity requirement by replacing the medium [71]. In this chapter, we use solids as a medium for harmonic generation. Due to the coupling among the atoms, the ionization potential becomes a bandgap. The bandgap in a solid is generally lower than the ionization potential of each individual atom, and the choice of material provides high flexibility in bandgap ranges. For example, ZnO has a bandgap of 3.3 eV, which reduces the requirement for the laser intensity down to 10^{12} $\mathrm{W/cm^2}$ [71].

5.1.3 Recollision in solids

Harmonic generation from solids can also be described using the three-step model. The recollision model of high harmonic generation from solids is the following:

1. An electron tunnels from the valence to the conduction band, leaving a hole in the valance band.
2. The laser field accelerates the electron-hole pair. Different from atoms, where the hole resides in the parent ion and does not move much in space, both the electron and the hole propagate in the solid. The energy increase depends on the band structure.

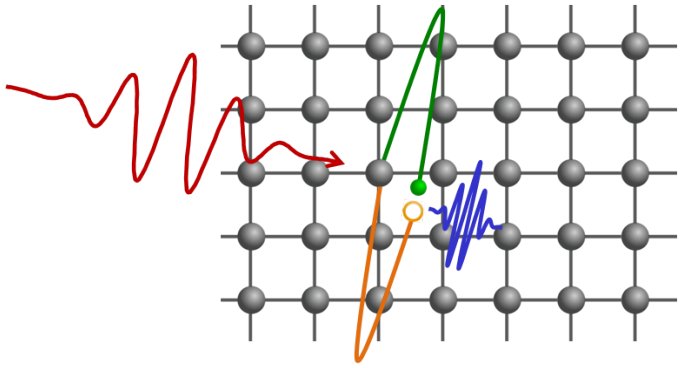

Figure 5.1: An intense laser pulse (red) is focused on a solid and create an electron-hole pair. The electron (green) and the hole (orange) are accelerated by the laser pulse. Upon recollision, a high-harmonic photon is emitted (blue). The displacement along the laser propagation direction is for illustration purpose.

3. If the electron-hole pair were generated at the right time in a laser cycle, they can re-encounter. They can recombine and emit a harmonic photon. The recombination also does not have to be at the same position where the electron-hole pair generated.

Although the smaller bandgap of solids such as silicon reduces the demand for laser intensities, it also requires laser pulses with longer wavelengths so that the absorption of the driving pulse is low. To generate harmonics from solids with a longer wavelength, previous experiments used difference frequency generation (DFG) of the signal and idler of an optical parametric amplifier (OPA) pumped by 800 nm pulses from a Ti:Sapphire system [72, 73].

In this chapter, we simplify harmonic generation from solids by using a fiber laser to generate harmonics from solids [21, 74]. A fiber laser is not only simpler than a Ti:Sapphire + OPA system or an enhancement cavity, but also more compact and financially friendly, and therefore has the potential for wide applications.

5.2 Driving with a fiber laser

5.2.1 Tm fiber laser

We use a thulium fiber laser that delivers 1.9 μm, 60 fs pulses at a repetition rate of 93.4 MHz. The average power of this laser is 1 W. The pulses emerge directly from a standard polarization-maintaining optical fiber and have very good mode quality. This laser can be turned into a frequency comb.

The beam coming out of the fiber laser is divergent, so we use a chalcogenide aspheric lens with a focal length of 4 mm to collimate the beam, and use another identical lens for focusing onto the sample. This symmetric arrangement is intended to reduce aberrations and provide a focus comparable to the fiber mode. We measured the mode size by knife edge, finding a 90/10 diameter of about 8 μm, but this value is quite sensitive to alignment. The peak intensity in these conditions would be over 10^{11} W/cm^2, but chromatic aberrations likely increase the pulse duration. Since there is further optimization of optical alignment while observing third harmonic generation, the final beam size may be smaller.

We optimize the alignment by maximizing the 3rd harmonic generation. We remove the fundamental beam with a highly reflective dielectric mirror and focus the harmonics. The 3rd harmonic of 1.9 μm, 633 nm, is red and it can easily be found with a white card. After the 3rd harmonic is found, we send the beam to a photodiode. Then we optimize the focus on the sample by carefully adjusting the position of the fiber end, which is on a 3D translation stage, as well as the position of the sample along the beam path, to maximize the power of the 3rd harmonic.

5.2.2 Harmonic detection

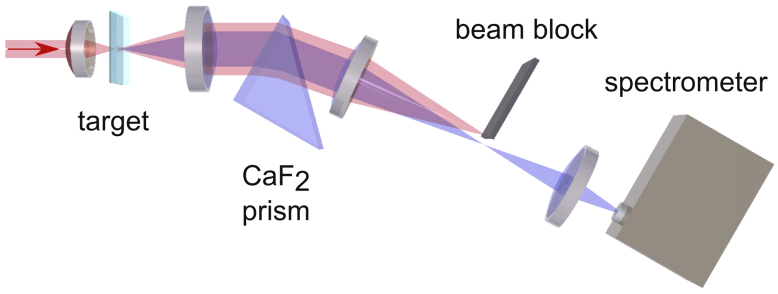

Figure 5.2: Layout of experiment optics. Harmonics are generated by focusing into a silicon or zinc oxide target, and separated by a prism to block the strong pump beam or strong low order harmonics from reaching the spectrometer.

After optimization, the generated harmonics, as well as the pump pulse, are collimated by a CaF_2 lens with a focal length of 20 mm. The 3rd harmonic is much stronger than the 5th and 7th harmonic, and requires a much shorter integration time to get a spectrum with a good signal-to-noise ratio. If we measure a spectrum with all the harmonics simultaneously, the 3rd harmonic will be saturated at an integration time long enough for the 5th. Moreover, the saturation of the 3rd harmonic raises the noise level at

other wavelengths, which makes it even more difficult to observe the higher harmonics. To avoid these problems, we use a CaF_2 prism to separate different wavelengths spatially.

After the prism, we focus the beams and block the pump beam at the focus with a twisted tube. The twisted tube acts like a beam dump to absorb the pump. We then refocus the harmonics into the ~100 μm slit of a CCD grating spectrometer (Ocean Optics USB2000+). Since different wavelengths are spatially separated, each order of harmonics requires a different optimal position of the spectrometer. This allows us to measure the weak high order harmonics without being overwhelmed by the bright low order harmonics, although comparison between different harmonics becomes difficult because they are not measured under the exact same conditions or simultaneously.

5.2.3 Harmonic spectra

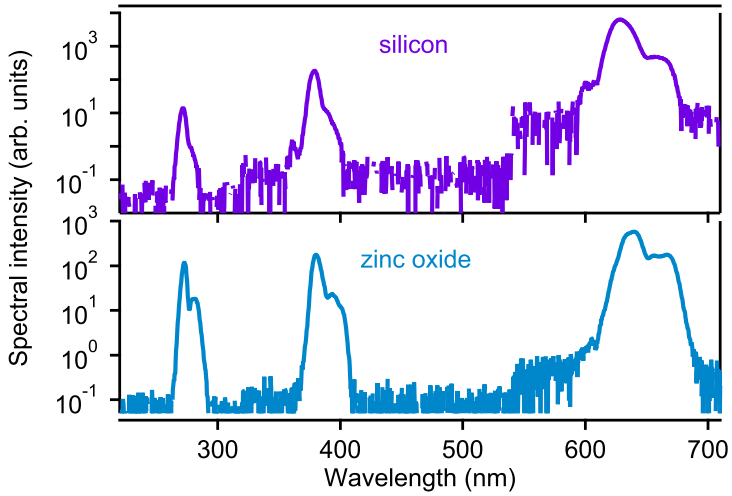

Figure 5.3: Spectra of the 7th, 5th, and 3rd harmonics of a 1 W thulium fiber laser generated in thin-film silicon and zinc oxide. Silicon has a 1.1 eV indirect, and 3.5 eV direct bandgap. Zinc oxide has a 3.3 eV direct bandgap.

We used two samples in the experiments: a 120 nm monocrystalline silicon film on 0.5 mm of sapphire substrate, and a 200 μm thick monocrystalline zinc oxide disk. Because the sapphire substrate of the silicon sample is birefringent, the driving laser pulse has to enter the sample from the silicon side to keep the polarization linear in the silicon film. To make sure the harmonics are generated from the silicon film, we tested with a 0.5 mm thick plain sapphire window under the same conditions. We confirmed that the plain sapphire window only produced a detectable 3rd harmonic. Therefore, any higher order harmonics are purely from the thin film.

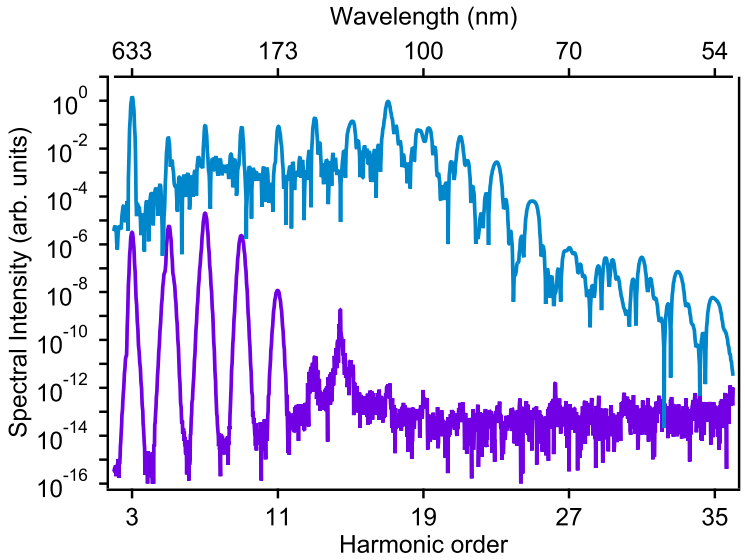

Figure 5.4: The purple, lower curve is a quantum calculation of the harmonic spectra from silicon near our experimental conditions. The blue, upper curve is for ZnO with a 6.25 times higher pump intensity and antireflection coating, indicating the possibility for photon generation in the 10 eV range.

Figure 5.3 shows spectra of harmonics generated from the two samples at the maximum pulse energy of the driving laser beam. Each harmonic is measured at its own optimal spectrometer position and scaled to the same integration time. In experiment, we observed a strong red beam of the 3rd harmonic. The 5th harmonic and the 7th harmonic from ZnO were also strong enough to saturate the spectrometer in several milliseconds of integration time. The shape of the spectrum changes slightly as we adjust the sample position, indicating chromatic aberration of the driving beam at the focus.

5.2.4 Simulation

We simulated the harmonic generation at an intensity of 6.6×10^{11} W/cm^2 before the pulse enters the samples. This intensity can be considered as an upper bound for the harmonic generation, since the actual intensity in the experiments might be lower than that due to aberrations. Results from semiclassical modeling of an electron-hole pair [75, 76] shows a harmonic cutoff at harmonic 7.8. Figure 5.4 shows predicted harmonic spectra by a quantum calculation. A cutoff at the 9th harmonic from the silicon sample is expected, as is shown in the purple curve in Fig. 5.4. The quantum calculation predicts a cutoff at a higher order harmonic because it includes the offset of the electron birth position relative to the hole, which is not included the semiclassical calculation.

Considering that future laser techniques will provide higher pulse energy, we calculated harmonic generation from ZnO at an intensity that is 6.25 times higher and also assume the sample has an anti-reflection coating. The calculation results, shown as the blue curve in Fig. 5.4, suggest the potential for generating 19th harmonic with a photon energy of 12 eV, or at the wavelength of 100 nm.

5.3 Damage tests

Material damage is often a limiting factor in harmonic generation from solids [77, 71], especially when the high repetition rate increases the laser fluence. In our experiments, the samples did not show any damage under a microscope, and we tested for damage in three ways and confirmed that we only observe thermal effects but no permanent damage.

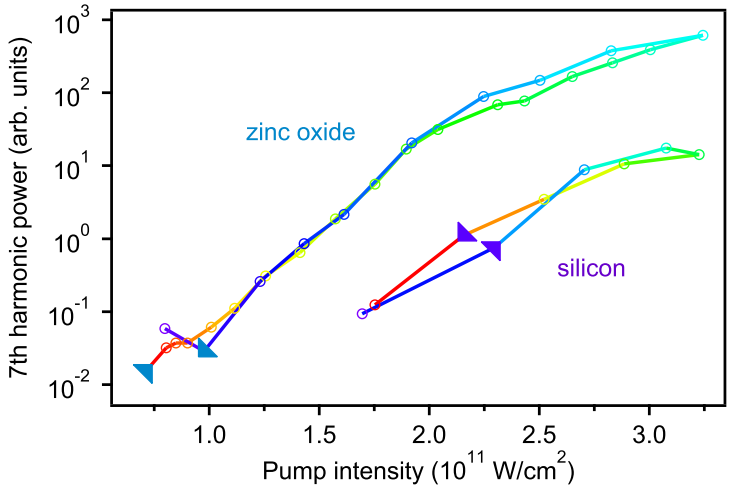

Figure 5.5: The 7th harmonic signal from zinc oxide and silicon integrated over the spectrum as the pump power is stepped up and back down, with direction indicated by the arrows. The repeatability in both directions indicates that the sample is not being damaged by the strong pump.

In the first test, we measure the intensity of the 7th harmonic by integrating its spectrum at different pump laser intensities, controlled by a neutral density filter. We start at a low intensity and increase it by steps to the maximum, and then decrease it by steps to our starting intensity. At each step, the samples were illuminated for tens of seconds. If the material is damaged at the high intensities, the harmonic signal when stepping down will be weaker than stepping up. Figure 5.5 shows the 7th harmonic

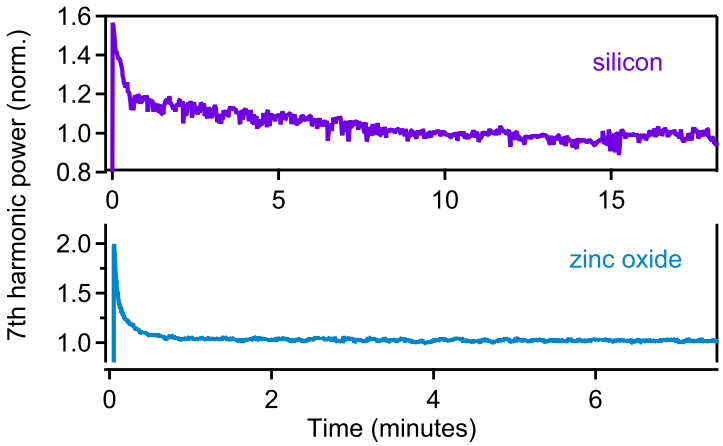

Figure 5.6: The 7th harmonic signal from zinc oxide and silicon integrated over the spectrum, taken over several minutes. There are early changes at thermal timescales, but the signal remains consistent, indicating either no damage, or no continuing damage.

signal remains the same, indicating the material is not damaged by the maximum pump intensity.

In the second test, we record the 7th harmonic over minutes and the results are shown in Fig. 5.6. The samples are illuminated from t=0. The harmonic signals are the strongest at t = 0, and decrease on a time scale of seconds, and stabilize after that. Although the decrease seems to be from damage, in some cases the harmonics output increases upon illumination, depending on the alignment. Therefore, we attribute it to thermal effects, possibly thermal lensing effects from the collection process, which can affect the alignment to the spectrometer.

In the third test, we record the intensity of the harmonics with a large CCD array instead of the spectrometer. The large detection area of a CCD array is good for avoiding alignment issue from focusing into a small slit. To reduce the pump laser in the harmonics, we use an 850 nm long pass filter to reflect the harmonics onto the camera. A red filter and a neutral density filter further reduces background light from the room. Mostly third harmonic is detected by the camera.

Figure 5.7 shows the harmonic signal from ZnO as we block and unblock the pump pulse over time. We observe a decrease in the signal over a few seconds, which is similar to the measurement with the spectrometer. However, blocking and unblocking the pump pulse recovers the signal. The recovery is small after blocking for a short time and full recovery can be achieved with a long blocking time. This suggests the sample was heated by the pump, and blocking the beam allows heat dissipation, and thus recovers

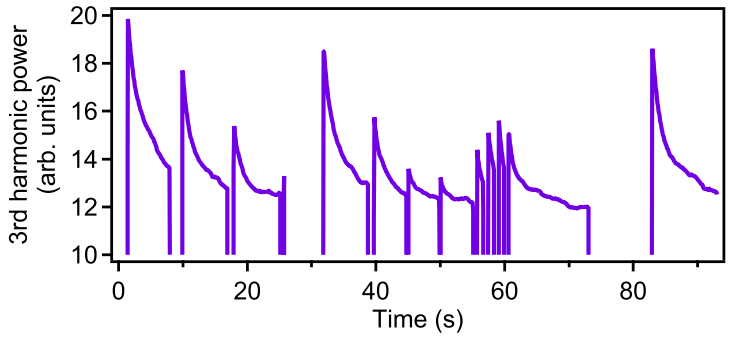

Figure 5.7: The 3rd harmonic signal from silicon with time while the pump beam is blocked for different periods. The decay and recovery of output depends on blocking time, consistent with heating from the pump, rather than accumulating damage.

the harmonic signal. This also implies that one can cool the samples to obtain stronger harmonics in experiments.

5.4 Summary

Combining harmonic generation with fiber lasers not only provides an opportunity to generate frequency combs at extreme ultraviolet through a simple setup, but also pave the way for industrial application of harmonics. In a recent study, harmonic generation has demonstrated potential for imaging the electric field in a circuit [24], which would have more widespread availability if using a fiber laser source.

In our experiments, we have shown that harmonic generation can be greatly simplified using a fiber laser. We generated up to the seventh harmonic from a thin film silicon sample and a zinc oxide sample. Heating affects the harmonic signal but no permanent damage is caused. The intensity of the harmonics can be improved in many ways, such as cooling, adding anti-reflection coating to the sample, or developing fiber lasers with higher pulse energy. Applying various solid engineering techniques such as nanostructures [77, 78] and doping [23], can also improve the efficiency of harmonic generation. Overall, generating harmonic from solids with fiber lasers is a promising technique from both scientific and industrial perspectives.

Chapter 6

Conclusion

Emergence is everywhere around us: snow emerges from water, dunes emerge from sand and wind, and the solar system emerged from a particular distribution of matter. The thesis that you are reading right now is also an emergent phenomenon – it arises from words combined in an order, and hopefully means more than individual words to readers. Just like one cannot become a good musician only from learning individual notes, a molecular system cannot be fully understood by only knowing individual atoms. In this thesis, we have explored three systems of increasing complexity through their interaction with strong laser pulses.

In the NO_2 molecule, a conical intersection emerges from coupling between nuclei and electrons. The conical intersection then perturbs the vibrational structure of the molecule, giving rise to chaotic vibronic degrees of freedom [36, 79]. This results in statistical characteristics in the photodissociation of NO_2. We directly measured the evolution of the NO-O molecular bond as the dissociation occurs. Similar photoreactions where the conical intersection is on the pathway between the photoexcited state and the products are common in polyatomic molecules [80]. One example is found in the photoisomerization of retinal [81], which works with the rhodopsin protein to allow you to see this thesis. Understanding these important reactions requires understanding of the complex statistical behaviors.

In the $(CO)_2$ dimer, a new dissociation channel emerges from interactions between the two component CO molecules in the van der Waals complex. This new channel arises from two effects. The first one is that the Coulomb field of CO^+ modifies the potential energy surface of the CO^+, and the second one is that the coupling between different charge state configurations gives rise to a new dimer electronic state. Such impacts should be considered in studying other van der Waals systems, which are ubiquitous in nature. For example, water molecules interact through hydrogen bonds, which are important for

all living systems. Base pairing in DNA is also through hydrogen bonds, which break and form during DNA replication. Beyond van der Waal complexes, the Coulomb interaction from a nearby ion can occur in any system with nearby ions. It has been demonstrated that the ionization rate can be enhanced by over an order of magnitude when another ion is nearby [82, 83]. Other systems that contain ions in vicinity to each other, for example lasing in air, can also be affected by the Coulomb field of the ions.

In solids, energy bands and a bandgap emerge from coupling among many atoms. The bandgap, which is generally lower than the ionization potential of individual atoms, lowers the laser intensity requirement for generating electron-hole pairs. We used this emergent property to generate harmonic radiation from solids with a fiber laser. Harmonic generation from solids is not only a new source for coherent radiation, but also provides new insights into interesting processes such as attosecond carrier dynamics in semiconductors and novel materials such as graphene [84] and MoS_2 [85].

We discovered, measured, and used emergent phenomena in three systems of different complexity. Emergent phenomena occur in everything, from particle physics to astronomy, chemistry, biology, and even sociology. This thesis is less than the tip of the iceberg, and there are more interesting and more complicated systems to be explored. As much as emergence is complex, this complexity is intriguing, making the world the spectacular place that it is.

Appendix A

Atomic units conversion

Constant	Formula	atomic units	SI units
electron mass	m_e	1	$9.1093836 \times 10^{-31}$ kg
elementary charge	e	1	$1.6021766 \times 10^{-19}$ C
reduced Planck's constant	$\hbar = h/(2\pi)$	1	$1.0545717 \times 10^{-34}$ J $\cdot$ s
Coulomb constant	$k_e = 1/(4\pi\epsilon)$	1	8.9875518×10^{9} N $\cdot$ m^2/C^2
atomic mass unit	amu $= \frac{1}{12}m(^{12}C)$	1822.89	$1.6605390 \times 10^{-27}$ kg
speed of light	c	137.04	2.9979245×10^{8} m/s

Dimension	Formula	SI units	Other common units
mass	m_e	$9.1093836 \times 10^{-31}$ kg	
charge	e	$1.6021766 \times 10^{-19}$ C	
length	a_0	$5.2917721 \times 10^{-11}$ m	
energy	$E_h = m_e e^4/(4\pi\epsilon\hbar)^2$	$4.3597441 \times 10^{-18}$ J	27.211385 eV, 2.19474×10^{5} cm^{-1}
time	$\hbar/E_h$	$2.4188843 \times 10^{-17}$ s	24.188843 attoseconds
momentum	$\hbar/a_0$	$1.9928519 \times 10^{-24}$ kg $\cdot$ m/s	
velocity	$a_0 E_h/\hbar$	2.1876912×10^{6} m/s	
electric field	$E_h/(ea_0)$	5.1422065×10^{11} V/m	51.422065 V/Å

Bibliography

[1] P. B. Corkum. Plasma perspective on strong field multiphoton ionization. *Phys. Rev. Lett.*, 71(13):1994, 1993.

[2] D. N. Fittinghoff, P. R. Bolton, B. Chang, and K. C. Kulander. Observation of nonsequential double ionization of helium with optical tunneling. *Phys. Rev. Lett*, 69:2642–2645, 1992.

[3] U. Mohideen, M. H. Sher, H. W. K. Tom, G. D. Aumiller, O. R. Wood II, R. R. Freeman, J. Boker, and P. H. Bucksbaum. High Intensity Above-Threshold Ionization of He. *Phys. Rev. Lett.*, 71(4):509–512, 1993.

[4] Heide Ibrahim1, Catherine Lefebvre1, André D Bandrauk, André Staudte, and François Légaré. H_2: the benchmark molecule for ultrafast science and technologies. *J. Phys. B: At. Mol. Opt. Phys.*, 51:042002, 2018.

[5] Andrew A. Lacis, Gavin A. Schmidt, David Rind, and Reto A. Ruedy. Atmospheric CO_2: Principal Control Knob Governing Earth's Temperature. *Science*, 330:356–359, 2011.

[6] J. Hansen, D. Johnson, A. Lacis, S. Lebedeff, P. Lee, D. Rind, and G. Russell. Climate Impact of Increasing Atmospheric Carbon Dioxide. *Science*, 213(4511):957–966, 1981.

[7] H. J. Wörner, J. B. Bertrand, D. V. Kartashov, P. B. Corkum, and D. M. Villeneuve. Following a chemical reaction using high-harmonic interferometry. *Nature*, 466(7306):604, 2010.

[8] H. J. Wörner, J. B. Bertrand, B. Fabre, J. Higuet, H. Ruf, A. Dubrouil, S. Patchkovskii, M. Spanner, Y. Mairesse, V. Blanchet, E. Mével, E. Constant, P. B. Corkum, and D. M. Villeneuve. Conical intersection dynamics in NO_2 probed by homodyne high-harmonic spectroscopy. *Science*, 334(6053):208, 2011.

[9] E. Frumker, C. T. Hebeisen, N. Kajumba, J. B. Bertrand, H. J. Wörner, M. Spanner, D. M. Villeneuve, A. Naumov, and P. B. Corkum. Oriented Rotational Wave-Packet

Dynamics Studies via High Harmonic Generation. *Phys. Rev. Lett.*, 109:113901, 2012.

[10] Marko Haertelt, Xue-Bin Bian, Michael Spanner, André Staudte, and Paul B. Corkum. Probing Molecular Dynamics by Laser-Induced Backscattering Holography. *Phys. Rev. Lett.*, 116:133001, 2016.

[11] Ruaridh Forbes, Andrey E. Boguslavskiy, Iain Wilkinson, Jonathan G. Underwood, and Albert Stolow. Excited state wavepacket dynamics in NO_2 probed by strong-field ionization. *J. Chem. Phys*, 147:054305, 2017.

[12] L. Drescher, M. C. E. Galbraith, G. Reitsma, J. Dura, N. Zhavoronkov, S. Patchkovskii, M. J. J. Vrakking, and J. Mikosch. Communication: XUV transient absorption spectroscopy of iodomethane and iodobenzene photodissociation. *J. Chem. Phys.*, 145:011101, 2016.

[13] Kevin F. Lee. *Controlling Molecular Alignment.* PhD thesis, McMaster University, 2006.

[14] F. Légaré, Kevin F. Lee, I. V. Litvinyuk, P. W. Dooley, S. S. Wesolowski, P. R. Bunker, P. Dombi, F. Krausz, A. D. Bandrauk, D. M. Villeneuve, and P. B. Corkum. Laser Coulomb-explosion imaging of small molecules. *Phys. Rev. A*, 71:013415, 2005.

[15] F. Légaré, Kevin F. Lee, I. V. Litvinyuk, P. W. Dooley, A. D. Bandrauk, D. M. Villeneuve, and P. B. Corkum. Imaging the time-dependent structure of a molecule as it undergoes dynamics. *Phys. Rev. A*, 72:052717, 2005.

[16] F. Légaré, Kevin F. Lee, P. W. Dooley, A. D. Bandrauk, D. M. Villeneuve, and P. B. Corkum. Laser Coulomb explosion imaging for probing ultra-fast molecular dynamics. *Journal of Physics B: Atomic, Molecular and Optical Physics*, 39:S503, 2006.

[17] Xiaoyan Ding, Kevin Lee, Andre Staudte, David M. Villeneuve, and Paul B. Corkum. Coulomb explosion imaging of NO_2 dissociation. Frontiers in Optics, The Optical Society of America, ISBN: 978-1-55752-987-9, 2013.

[18] L. M. Woods, D. A. R. Dalvit, A. Tkatchenko, P. Rodriguez-Lopez, A. W. Rodriguez, and R. Podgornik. Materials perspective on Casimir and van der Waals interactions. *Rev. Mod. Phys.*, 88(4):045003, 2016.

[19] F. Trinter, M. S. Schöffler, H.-K. Kim, F. P. Sturm, K. Cole, N. Neumann, A. Vredenborg, J. Williams, I. Bocharova, R. Guillemin, M. Simon, A. Belkacem, A. L. Landers, Th. Weber, H. Schmidt-Böcking, R. Dörner, and T. Jahnke. Resonant auger decay driving intermolecular coulombic decay in molecular dimers. *Nature*, 505:664, 2014.

[20] L.S. Cederbaum, J. Zobeley, and F. Tarantelli. Giant Intermolecular Decay and Fragmentation of Clusters. *Phys. Rev. Lett.*, 79(24):4778–4781, 1997.

[21] Kevin F. Lee, Xiaoyan Ding, T. J. Hammond, M. E. Fermann, G. Vampa, and P. B. Corkum. Harmonic generation in solids with direct fiber laser pumping. *Optics Letters*, 42(6):1113–1116, 2017.

[22] Nicolas Tancogne-Dejean, Oliver D. Mücke, Franz X. Kärtner, and Angel Rubio. Ellipticity dependence of high-harmonic generation in solids originating from coupled intraband and interband dynamics. *Nature Communications*, 8(745), 2017.

[23] Murat Sivis, Marco Taucer, Giulio Vampa, Kyle Johnston, Andre Staudte, Andrei Yu. Naumov, D. M. Villeneuve, Claus Ropers, and P. B. Corkum. Tailored semiconductors for high-harmonic optoelectronics. *Science*, 357:303–306, 2017.

[24] G. Vampa, T. J. Hammond, M. Taucer, Xiaoyan Ding, X. Ropagnol, T. Ozaki, S. Delprat, M. Chaker, N. Thiré, B. E. Schmidt, F. Légaré, D. D. Klug, A. Yu. Naumov, D. M. Villeneuve, A. Staudte, and P. B. Corkum. Strong-field optoelectronics in solids. *Nature Photonics*, 12:465–468, 2018.

[25] J. Ullrich, R. Moshammer, A. Dorn, R. Dörner, L. Ph. H. Schmidt, and H. Schmidt-Böcking. Recoil-ion and electron momentum spectroscopy: reaction-microscopes. *Rep. Prog. Phys.*, 66:1463, 2003.

[26] André Staudte. *Subfemtosecond Electron Dynamics of H_2 in Strong Fields or The Quest for the Molecular Clock*. PhD thesis, der Johann Wolfgang Goethe – Universität, 2005.

[27] Moritz Meckel. Strong-Field Ionization of Aligned Oxygen Molecules. Masters thesis, Johann Wolfgang Goethe Universität, 2006.

[28] Ottmar Jagutzki et al. Multiple Hit Readout of a Microchannel Plate Detector With a Three-Layer Delay-Line Anode. *IEEE Transactions on Nuclear Science*, 49(5):2477–2483, 2002.

[29] I. V. Litvinyuk, Kevin F. Lee, P. W. Dooley, D. M. Rayner, D. M. Villeneuve, and P. B. Corkum. Alignment-dependent strong field ionization of molecules. *Phys. Rev. Lett*, 90:233003, 2003.

[30] Barbara J. Finlayson-Pitts and James N. Pitts Jr. Tropospheric Air Pollution: Ozone, Airborne Toxics, Polycyclic Aromatic Hydrocarbons, and Particles. *Science*, 276(5315):1045–1051, 1997.

[31] H. Gaedtke and J. Troe. Primary Processes in the Photolysis of NO_2. *Ber. Bunsenges. Phys. Chem.*, 79:184–191, 1975.

[32] I. Wilkinson and B. J. Whitaker. Some remarks on the photodynamics of NO_2. *Annu. Rep. Prog. Chem., Sect. C: Phys. Chem.*, 106:274, 2010.

[33] Y. Arasaki and K. Takatsuka. Quantum wavepacket dynamics for time-resolved photoelectron spectroscopy of the NO_2 conical intersection. *Chem. Phys.*, 338:175–185, 2007.

[34] D. Reignier, T. Stoecklin, P. Halvick, A. Voronin, and J. C. Rayez. Analytical global potential energy surfaces of the two lowest ^{2}A' states of NO_2. *Phys. Chem. Chem. Phys.*, 3:2726, 2001.

[35] Rémy Jost, Jesper Nygård, Adam Pasinski, and Delon Antoine. The photodissociation threshold of NO_2: Precise determination of its energy and density of states. *J. Chem. Phys.*, 105(3):1287–1290, 1996.

[36] Patrick Dupré. Photodissociation resonances of jet-cooled NO_2 at the dissociation threshold by CW-CRDS. *J. Chem. Phys.*, 142:174305, 2015.

[37] M. Kawasaki, H. Sato, A. Fukuroda, T. Kikuchi, S. Kobayashi, and T. Arikawa. Angular distributions of photofragments from NO_2 photodissociation. *J. Chem. Phys*, 86(8):4431, 1987.

[38] D.C. Robie, M. Hunter, J.L. Bates, and H. Reisler. Product state distributions in the photodissociation of expansion-cooled NO_2 near the $NO(X^3\Pi)$ $v = 1$ threshold. *Chem. Phys. Lett.*, 193(5):413, 1992.

[39] M. Hunter, S. A. Reid, D. C. Robie, and H. Reisler. The monoenergetic unimolecular reaction of expansion-cooled NO_2: NO product state distributions at excess energies 0–3000 cm^{-1}. *J. Chem. Phys*, 99:1093, 1993.

[40] A. Vredenborg, W. G. Roeterdink, and M. H. M. Janssen. Femtosecond time-resolved photoelectron-photoion coincidence imaging of multiphoton multichannel photodynamics in NO_2. *J. Chem. Phys.*, 128(20):204311, 2008.

[41] J. B. Hamard, R. Cireasa, B. Chatel, V. Blanchet, and B. J. Whitaker. Quantum interference in NO_2. *J. Phys. Chem. A*, 114(9):3167, 2010.

[42] R. Schinke, S.Yu. Grebenshchikov, and H. Zhu. The photodissociation of NO_2 in the second absorption band: *Ab initio* and quantum dynamics calculations. *Chemical Physics*, 346:99, 2008.

[43] R.H. Dalitz. Decay of τ Mesons of Known Charge. *Phys. Rev.*, 94(4):1046–1051, 1954.

[44] Akitaka Matsuda, Eiji J. Takahashi, and Akiyoshi Hishikawa. Dalitz plot analysis of Coulomb exploding O_3 in ultrashort intense laser fields. *J. Chem. Phys.*, 127:114318, 2007.

[45] Benji Wales, Tomonori Motojima, Jun Matsumoto, ZiJian Long, Wing-Ki Liu, Haruo Shiromaru, and Joseph Sanderson. Multiple ionization and complete fragmentation of OCS by impact with highly charged ions Ar^{4+} and Ar^{8+} at 15 keV q^{-1}. *J. Phys. B: At. Mol. Opt. Phys.*, 45:045205, 2012.

[46] Shigeki Kawai, Adam S. Foster, Torbjörn Björkman, Sylwia Nowakowska, Jonas Björk, Filippo Federici Canova, Lutz H. Gade, Thomas A. Jung, and Ernst Meyer. Van der Waals interactions and the limits of isolated atom models at interfaces. *Nature Communications*, 7(11559), 2016.

[47] U. Frühling, F. Trinter, F. Karimi, J.B. Williams, and T. Jahnke. *Journal of Electron Spectroscopy and Related Phenomena*, 204:237, 2015.

[48] T. Jahnke, H. Sann, T. Havermeier, K. Kreidi, C. Stuck, M. Meckel, M. Schöffler, N. Neumann, R.Wallauer, S. Voss, A. Czasch, O. Jagutzki, A. Malakzadeh, F. Afaneh, Th. Weber, H. Schmidt-Böcking, and R. Dörner. Ultrafast energy transfer between water molecules. *Nat. Phys.*, 6:139, 2010.

[49] Xiaoyan Ding, M. Haertelt, S. Schlauderer, M. S. Schuurman, A. Yu. Naumov, D. M. Villeneuve, A. R. W. McKellar, P. B. Corkum, and A. Staudte. Ultrafast Dissociation of Metastable CO^{2+} in a Dimer. *Phys. Rev. Lett*, 118:153001, 2017.

[50] Mojtaba Rezaei, S. Sheybani-Deloui, N. Moazzen-Ahmadi, K. H. Michaelian, and A. R. W. McKellar. CO Dimer: The Infrared Spectrum Revisited. *J. Phys. Chem. A*, 117:9612, 2013.

[51] Richard Dawes, Xiao-Gang Wang, and Tucker Carrington. CO Dimer: New Potential Energy Surface and Rovibrational Calculations. *J. Phys. Chem. A*, 117:7612, 2013.

[52] L. H. Andersen, J. H. Posthumus, O. Vahtras, H. Agren, N. Elander, A. Nunez, A. Scrinzi, M. Natiello, and M. Larsson. Very Slow Spontaneous Dissociation of CO^{2+} Observed by Means of a Heavy Ion Storage Ring. *Phys. Rev. Lett.*, 71:1812, 1993.

[53] M. Lundqvist, P. Baltzer, D. Edvardsson, L. Karlsson, and B. Wannberg. Novel Time of Flight Instrument for Doppler Free Kinetic Energy Release Spectroscopy. *Phys. Rev. Lett.*, 75:1058, 1995.

[54] M. Hochlaf, R. I. Hall, F. Penent, H. Kjeldsen, P. Lablanquie, M. Lavollée, and J. H. D. Eland. Threshold photoelectrons coincidence spectroscopy of N_2^{2+} and CO^{2+} ions . *Chem. Phys.*, 207:159, 1996.

[55] J. P. Bouhnik, I. Gertner, and B. Rosner. Measurements of the mean lifetime and kinetic-energy release of metastable CO^{2+}. *Phys. Rev. A*, 63:032509, 2001.

[56] T. Šedivcová, P. R. Ždánská, and V. Špirko. Computed lifetimes of metastable states of CO^{2+}. *J. Chem. Phys.*, 124:214303, 2006.

[57] Felicja Mrugała. A computational study of metastable states of CO^{2+}. *J. Chem. Phys.*, 129:064314, 2008.

[58] S. De, M. Magrakvelidze, I. A. Bocharova, D. Ray, W. Cao, I. Znakovskaya, H. Li, Z. Wang, G. Laurent, U. Thumm, M. F. Kling, I. V. Litvinyuk, I. Ben-Itzhak, and C. L. Cocke. Following dynamic nuclear wave packets in N_2, O_2, and CO with few-cycle infrared pulses. *Phys. Rev. A*, 84:043410, 2011.

[59] F. Penent, R. I. Hall, R. Panajotović, J. H. D. Eland, G. Chaplier, and P. Lablanquie. New Method for the Study of Dissociation Dynamics of State-Selected Doubly Charged Ions: Application to CO^{2+}. *Phys. Rev. Lett.*, 81:3619, 1998.

[60] X. Gong, M. Kunitski, L. Ph. H. Schmidt, T. Jahnke, A. Czasch, R. Dörner, and J. Wu. Simultaneous probing of geometry and electronic orbital of ArCO by Coulomb-explosion imaging and angle-dependent tunneling rates. *Phys. Rev. A*, 88:013422, 2013.

[61] John H. D. Eland et al. Photo double ionization spectra of CO: comparison of theory with experiment. *J. Phys. B: At. Mol. Opt. Phys*, 37:3197–3214, 2004.

[62] H. Lischka, R. Shepard, R. M. Pitzer, I. Shavitt, M. Dallos, Th. Müller, P. G. Szalay, M. Seth, G. S. Kedziora, S. Yabushita, and Z. Zhang. High-level multireference methods in the quantum-chemistry program system COLUMBUS: Analytic MR-CISD and MR-AQCC gradients and MR-AQCC-LRT for excited states, GUGA spin–orbit CI and parallel CI density. *Phys. Chem. Chem. Phys.*, 3:664, 2001.

[63] H. Lischka et al. Columbus, an ab initio electronic structure program, release 7.0, 2012.

[64] S.V. Levchenko, Hanna Reisler, Anna I. Krylov, Oliver Gessner, Albert Stolow, Huancong Shi, and Allan L. L. East. Photodissociation dynamics of the NO dimer. I. Theoretical overview of the ultraviolet singlet excited states. *J. Chem. Phys.*, 125:084301, 2006.

[65] Mathew Britton, Patrick Laferriere, Abdulaziz Alqasem, Ladan Arissian, and P.B. Corkum. N_2^+ gain in a pulsed gas jet. International Conference on Laser Filamentation, 2018.

[66] Tamar Seideman, M. Yu. Ivanov, and P. B. Corkum. The use of intese-field ionization in time-resolved measurements. *Chemical Physics Letters*, 252:181–188, 1996.

[67] Susan Jones, David T. A. Daley, Nicholas M. Luscombe, Helen M. Berman, and Janet M. Thornton. Protein–RNA interactions: a structural analysis. *Nucleic Acids Res.*, 29(4):943–954, 2001.

[68] Graham A. Rance, Dan H. Marsh, Stephen J. Bourne, Thomas J. Reade, and Andrei N. Khlobystov. van der Waals Interactions between Nanotubes and Nanoparticles for Controlled Assembly of Composite Nanostructures. *ACS Nano*, 4(8):4920—-4928, 2010.

[69] Christoph Gohle, Thomas Udem, Maximilian Herrmann, Jens Rauschenberger, Ronald Holzwarth, Hans A Schuessler, Ferenc Krausz, and Theodor W Hänsch. A frequency comb in the extreme ultraviolet. *Nature*, 436(7048):234–237, 2005.

[70] Arman Cingöz, Dylan C Yost, Thomas K Allison, Axel Ruehl, Martin E Fermann, Ingmar Hartl, and Jun Ye. Direct frequency comb spectroscopy in the extreme ultraviolet. *Nature*, 482(7383):68–71, 2012.

[71] Shambhu Ghimire, Anthony D DiChiara, Emily Sistrunk, Pierre Agostini, Louis F DiMauro, and David A Reis. Observation of high-order harmonic generation in a bulk crystal. *Nature Physics*, 7(2):138–141, 2011.

[72] G. Vampa, T.J. Hammond, N. Thiré, B.E. Schmidt, F. Légaré, C.R. McDonald, T. Brabec, and P.B. Corkum. Linking high harmonics from gases and solids. *Nature*, 522(7557):462–464, 2015.

[73] Giulio Vampa. *Role of Electron-hole Recollisions in High Harmonic Generation from Bulk Crystals*. PhD thesis, University of Ottawa, 2016.

[74] Kevin F. Lee, Xiaoyan Ding, T. J. Hammond, M. E. Fermann, G. Vampa, and P. B. Corkum. Harmonic generation in solids with direct fiber laser pumping. CLEO, IEEE, INSPEC Accession Number: 17291739, 2017.

[75] G. Vampa, C. R. McDonald, G. Orlando, D. D. Klug, P. B. Corkum, and T. Brabec. Theoretical analysis of high-harmonic generation in solids. *Phys. Rev. Lett.*, 113:073901, Aug 2014.

[76] G. Vampa, C. R. McDonald, G. Orlando, P. B. Corkum, and T. Brabec. Semiclassical analysis of high harmonic generation in bulk crystals. *Phys. Rev. B*, 91:064302, Feb 2015.

[77] G. Vampa, B. G. Ghamsari, S. Siadat Mousavi, T. J Hammond, A. Olivieri, E. Lisicka-Skrek, A. Yu Naumov, D. M. Villeneuve, A. Staudte, P. Berini, and P. B. Corkum. Plasmon enhanced high harmonic generation from silicon. *Nature Physics*, 13:659–662, 2017.

[78] Seunghwoi Han, Hyunwoong Kim, Yong Woo Kim, Young-Jin Kim, Seungchul Kim, In-Yong Park, and Seung-Woo Kim. High-harmonic generation by field enhanced femtosecond pulses in metal-sapphire nanostructure. *Nature Communications*, 7, 2016.

[79] R. Jost, G. Michalski, and M. Thiemens. Comparison of rovibronic density of asymmetric versus symmetric NO_2 isotopologues at dissociation threshold: Broken symmetry effects. *J. Chem. Phys.*, 123:054320, 2005.

[80] Graham A. Worth and Lorenz S. Cederbaum. Beyond Born-Oppenheimer: Molecular Dynamics Through a Conical Intersection. *Annu. Rev. Phys. Chem.*, 55:127–158, 2004.

[81] M. Garavelli, P. Celani, F. Bernardi, M. A. Robb, and M. Olivucci. The $C_5H_6NH_2^+$ Protonated Shiff Base: An *ab Initio* Minimal Model for Retinal Photoisomerization. *J. Am. Chem. Soc.*, 119:6891–6901, 1997.

[82] Tamar Seideman, M. Yu. Ivanov, and P. B. Corkum. Role of electron localization in intense-field molecular ionization. *Phys. Rev. Lett*, 75(15):2819–2822, 1995.

[83] E Constant, H Stapelfeldt, and P.B. Corkum. Observation of enhanced ionization of molecular ions in intense laser fields. *Phys. Rev. Lett*, 76(22):4140–4143, 1996.

[84] M. Taucer, T. J. Hammond, P. B. Corkum, G. Vampa, C. Couture, N. Thiré, B. E. Schmidt, F. Légaré, H. Selvi, N. Unsuree, B. Hamilton, T. J. Echtermeyer, and M. A. Denecke. Nonperturbative harmonic generation in graphene from intense midinfrared pulsed light. *Phys. Rev. B.*, 96:195420, 2017.

[85] Hanzhe Liu, Yilei Li, Yong Sing You, Shambhu Ghimire, Tony F. Heinz, and David A. Reis. High-harmonic generation from an atomically thin semiconductor. *Nature Physics*, 13:262–265, 2017.